https://doi.org/10.3847/1538-4357/ab67c9

ALMA Observations of Two Massive and Dense MALT90 Clumps

Sudeep Neupane[1] , Guido Garay[1], Yanett Contreras[2] , Andrés E. Guzmán[3] , and Luis Felipe Rodríguez[4]

[1] Departamento de Astronomía, Universidad de Chile, Camino el Observatorio 1515, Las Condes, Santiago, Chile; sneupane@das.uchile.cl
[2] Leiden Observatory, Leiden University, P.O. Box 9513, NL-2300 RA Leiden, The Netherlands
[3] NAOJ, Chile Observatory, East Asia ALMA Regional Center, Mitaka, Tokyo 181-8588, Japan
[4] Instituto de Radioastronomía y Astrofísica, Universidad Nacional Autónoma de México, Apdo. Postal 3-72 (Xangari), 58090 Morelia, Michoacán, México

Abstract

We report Atacama Large Millimeter Array observations of 3 mm dust continuum emission and line emission, in HCO^+, $H^{13}CO^+$, N_2H^+, and CH_3CN, toward two massive and dense clumps (MDCs) in early but distinct evolutionary phases (prestellar and protostellar), made with the goal of investigating their fragmentation characteristics at angular scales of $\sim 1''$. Toward the prestellar clump we detected 10 compact structures (cores), with radii from 1200–4500 au and masses from 1.6–20 $M_\odot$. Half of these cores exhibit inverse P Cygni profiles in HCO^+ and are subvirialized indicating that they are undergoing collapse. Toward the protostellar clump we detected a massive (119 $M_\odot$) central core, with a strong mass infall rate, and nine less massive cores, with masses from 1.7–27 $M_\odot$ and radii from 1000–4300 au. CH_3CN rotational temperatures were derived for eight cores in the protostellar clump and three cores in the prestellar clump. Cores within the prestellar clump have smaller line widths and lower temperatures than cores within the protostellar clump. The fraction of total mass in cores to clump mass is smaller in the prestellar clump ($\sim 6\%$) than in the protostellar clump ($\sim 23\%$). We conclude that we are witnessing the evolution of the dense gas in globally collapsing MDCs; the prestellar clump illustrating the initial stage of fragmentation, harboring cores that are individually collapsing, and the protostellar clump reflecting a later stage in which a considerable fraction of the gas has been gravitationally focused into the central region.

Unified Astronomy Thesaurus concepts: Interstellar medium (847); Star formation (1569); Massive stars (732); Collapsing clouds (267)

1. Introduction

A wealth of observations have shown that filamentary structures are ubiquitous within molecular clouds (e.g., Schneider & Elmegreen 1979; Myers 2009; André et al. 2010; Molinari et al. 2010). These long molecular structures are inhomogeneous and present overdensities, most likely a result of fragmentation (e.g., Takahashi et al. 2013; Contreras et al. 2016; Teixeira et al. 2016). It is in the most massive ($\sim 10^3 \, M_\odot$) and dense ($\sim 10^4 \, cm^{-3}$) overdensities, which we refer to as massive and dense clumps (or MDCs), where high-mass stars form (Faúndez et al. 2004; Contreras et al. 2017). However, the early evolution of MDCs and the ensuing fragmentation leading to the formation of cores is not well understood. The relative importance of primordial clump fragmentation versus large-scale accretion in determining the distribution of core masses still remains to be assessed. Recent Atacama Large Millimeter Array (ALMA) observations with moderate angular resolution ($\sim 3.5''$) toward a sample of MDCs in early evolutionary stages (infrared quiet) with masses in the range from 200–2000 $M_\odot$ revealed limited fragmentation at the scale of ~ 0.1 pc, showing typically ~ 3 cores, and a high efficiency in the formation of high-mass cores (Csengeri et al. 2017). Observations with higher resolution (~ 0.03–0.05 pc) of clumps with similar characteristics show a range of substructures—from a few fragments (e.g., Peretto et al. 2013; Sanhueza et al. 2017) to 10 or more fragments (e.g., Contreras et al. 2018; Lu et al. 2018). Some works concluded that the fragmentation properties of clumps are described by gravo-turbulence (e.g., Zhang et al. 2015), while others find them consistent with pure thermal Jeans fragmentation (e.g., Palau et al. 2015, 2018; Sanhueza et al.

2019). Teixeira et al. (2016) found that the separation of clumps within a filamentary cloud is consistent with the Jeans length of the filament, while the separation between the individual cores within the clumps is smaller than the Jeans length of the clump, which they suggest indicates that the local collapse of the clumps occurs at a much faster pace than the global collapse of the filament.

Determining the physical and kinematical properties of the molecular gas in MDCs at both, the large clump scale (~ 1 pc) and small core scale (5000 au), will permit investigating the presence of global or localized collapse and the characteristics of the primordial fragmentation. These properties together constitute a key discriminator between current models of the fragmentation and evolution of MDCs, such as competitive accretion (Bonnell & Bate 2006), turbulent fragmentation (Padoan & Nordlund 2002), and hierarchical gravitational fragmentation (Vázquez-Semadeni et al. 2009, 2017).

In this work we present a study of two MDCs, one in the prestellar stage and the other in the protostellar stage of evolution, using high resolution ALMA Band 3 continuum and molecular line observations with the goal of identifying and determining the physical characteristics of the dense and compact structures within the MDCs and to test models of the fragmentation and evolution of MDCs, and possibly to guide future theories. In Section 2, we briefly review the characteristics of the observed MDCs. In Sections 3 and 4, we describe the observations and present the results, respectively. In Section 5, we discuss the analysis of the continuum and molecular observations. In Section 6, we compare our results with the predictions of different models.
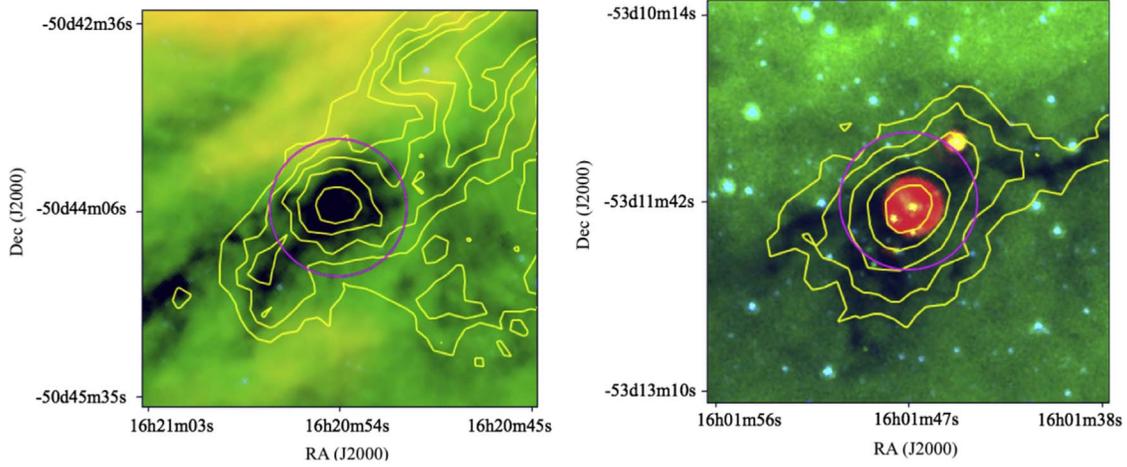
Figure 1. Three color *Spitzer* images (blue: 3.6 μm, green: 8 μm, and red: 24 μm) (Infrared Array Camera; Fazio et al. 2004, MIPS: Rieke et al. 2004) of the MALT90 targets overlaid with contours of the 870 μm emission from the Atlasgal survey (FWHM $\sim 20''$). The magenta circle indicates the ALMA primary beam (FWHM) of $\sim 62''$ in Band 3. Left panel: prestellar clump AGAL333. Contour levels are drawn at 3σ, 5σ, 7σ, 9σ, and 11σ ($\sigma = 93.3$ mJy beam^{-1}). Right panel: protostellar clump AGAL329. Contour levels are drawn at 3σ, 6σ, 12σ, 24σ, and 48σ ($\sigma = 89.3$ mJy beam^{-1}).

2. The Targets

The two MDCs studied in this work were selected from the MALT90[5] catalog (Rathborne et al. 2016), one AGAL333.014-0.521 (hereafter AGAL333) classified as been in the prestellar stage and the other AGAL329.184-0.314 (hereafter AGAL329) classified in the protostellar stage of evolution (see Figure 1). The MALT90 project (Foster et al. 2011; Jackson et al. 2013) surveyed, with the Mopra telescope, the emission in 15 different molecular lines (mostly $J = 1 \rightarrow 0$ transitions) and one recombination line toward $\sim$3200 MDCs. Toward AGAL329 and AGAL333 emission was detected in, respectively, nine and eight lines, including the high density tracers HCO$^+$, HNC, HCN, and N$_2$H$^+$. The $J = 1 \rightarrow 0$ transitions of these four species have critical densities[6] of the order of 10^5–10^6 cm^{-3} for a temperature of 20 K, indicating that the clumps indeed have high densities, a requisite for the formation of high-mass stars. The spectra of the optically thick HCO$^+$ emission from the protostellar clump shows a double peak profile, with the blueshifted peak being stronger than the redshifted peak, while the spectra of the optically thin H^{13}CO$^+$ emission shows a single line with a peak velocity in between the velocities of the blue and red peaks of the HCO$^+$ line. These profile characteristics are signposts of infall motions (e.g., Anglada et al. 1987; Mardones et al. 1997; De Vries & Myers 2005) suggesting that AGAL329 is undergoing a large-scale collapse. On the other hand, the profiles of the HCO$^+$ and H^{13}CO$^+$ emissions from the prestellar clump are nearly Gaussian, indicating a more static, quiescent region. As expected, SiO emission, which traces outflow/shocked gas (e.g., Martin-Pintado et al. 1992), is only detected toward AGAL329.

Table 1 lists the observed and derived parameters of the clumps. The velocities and line widths correspond to those determined from the HF fitting of the N$_2$H$^+$ emission as observed with the Mopra telescope in the MALT90 survey. The dust temperatures were determined by us from a fit to the

Table 1
Observed and Derived Parameters of the Clumps

Parameter	AGAL333.014-0.521	AGAL329.184-0.314	Reference
Clump type	Prestellar	Protostellar	(1)
Distance (kpc)	3.72	3.46	(2)
V_{lsr} (km s^{-1})	-53.8	-50.5	(1)
Line width (km s^{-1})	3.1	3.4	(1)
$F_{870\,\mu m}$ (Jy)	16.42	23.02	(3), (4)
θ ($'' \times ''$)	43×17	24×15	(3), (4)
Size (pc)	0.49	0.32	(5)
T_{dust} (K)	22	28	(5)
M_{dust} ($M_\odot$)	1080	940	(5)
$n(H_2)$ (10^5cm^{-3})	0.32	1.00	(5)
M_{vir} ($M_\odot$)	980	770	
α_{vir}	0.91	0.82	
Jeans mass ($M_\odot$)	6.8	5.5	
Jeans radius (pc)	0.09	0.06	

References. (1) Rathborne et al. (2016); (2) Whitaker et al. (2017); (3) Contreras et al. (2013); (4) Urquhart et al. (2014); (5) this work.

spectral energy distributions (SEDs), shown in Figure 2, using a single temperature modified blackbody model (see, Guzmán et al. 2015; König et al. 2017),

$$S_\nu = \Omega_s B_\nu(T_d)(1 - e^{-\tau_\nu}),\tag{1}$$

where S_ν, B_ν, T_d, and Ω_s are, respectively, the flux density, Planck function, dust temperature, and effective solid angle subtended by the clump. We assume that the dependence of the optical depth, τ_ν, with frequency ν can be expressed as

$$\tau = (\nu/\nu_o)^\beta,\tag{2}$$

where ν_o is the frequency at which the dust opacity is unity and β is the spectral index of the dust absorption coefficient.

The data points at infrared wavelengths (70–500 μm; red circles) were obtained from the Hi-Gal images (Molinari et al. 2010) available in the *Herschel* Science Archive and the data point at 850 μm (black square) was obtained from ATLASGAL images (Schuller et al. 2009). The fluxes were extracted using simple

---

5 The Millimetre Astronomy Legacy Team 90 GHz Survey: http://malt90.bu.edu.
6 Defined as, $n_{crit} = A_{ul}/\gamma_{ul}$, where A_{ul} is the Einstein coefficient and γ_{ul} is the collisional rate.
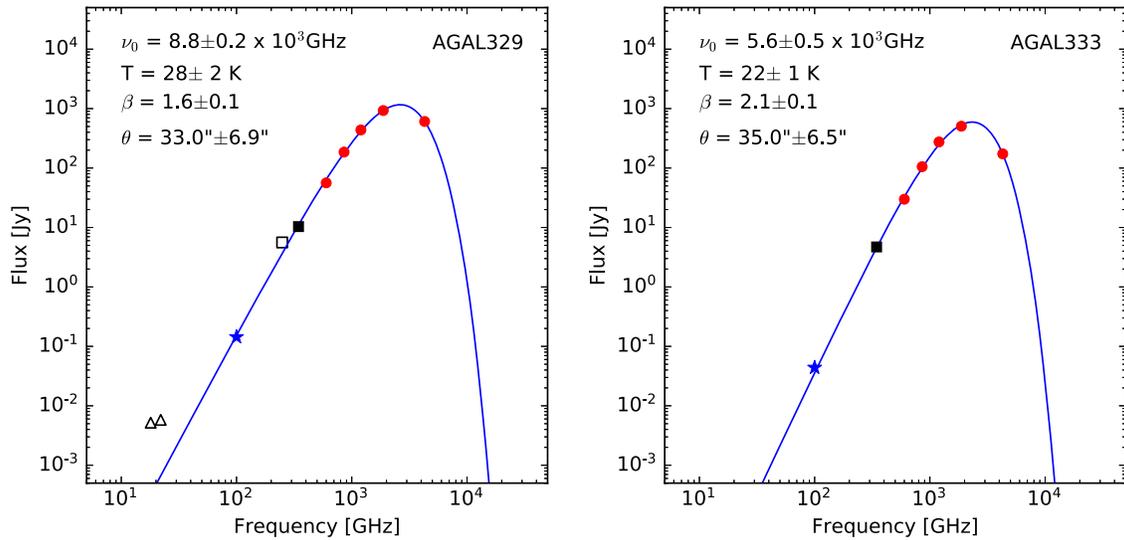
Figure 2. SED of clumps AGAL329 (left) and AGAL333 (right). The symbols are described in the text. The continuous lines (blue) correspond to the SEDs fit obtained from a least squares method. The fitted parameters are given inside each box.

aperture photometry of a circular region with radii of $27''$ and $20''$ for the prestellar and protostellar clumps, respectively. Errors in the flux densities, mostly due to calibration uncertainties, are less than 30%. Error bars are then smaller than the size of the symbols. Also incorporated in the SED are the flux densities measured at 100 GHz using the Atacama Compact Array (ACA) alone (present work; blue stars) and for the protostellar clump the 1.2 mm flux density reported by Beltrán et al. 2006 (open square). A least squares fit to the SED, using the SciPy optimize module in Python (Virtanen et al. 2019), gave values of T_d and β of 22 K and 2.1 for the prestellar clump and 28 K and 1.6 for the protostellar clump. Shown in the SED of the protostellar clump (Figure 2—left panel) are the flux densities at 18 and 22 GHz observed with the ATCA (Sánchez-Monge et al. 2013; triangles). These flux densities are well above those expected from the dust emission model, and most likely correspond to free–free emission from either a UC H II region or a region of shocked gas.

The clump size, mass, and density, given in lines 7, 9, and 10 in Table 1, were derived from the 870 μm continuum emission. The last two parameters were computed using the dust temperatures derived from the SED, a dust absorption coefficient of 1.85 cm^2 gr^{-1} (Ossenkopf & Henning 1994), and a gas-to-dust ratio of 100. The virial masses, $M_{vir} = 5\sigma^2 R/G$, where $\sigma = \Delta V/(8\ln2)^{1/2}$, are 980 $M_\odot$ for the prestellar clump and 770 $M_\odot$ for the protostellar clump. The virial parameter, defined as $\alpha_{vir} = M_{vir}/M_{dust}$, is 0.91 for the prestellar clump and 0.82 for the protostellar clump, suggesting that both of them are gravitationally bound. Also given in Table 1 are the Jeans mass and Jeans radius at the average temperature and density for both clumps.

In summary, the clumps selected for this study, which are at similar distances from the Sun, have masses, sizes, and densities characteristics of high-mass star-forming regions and their virial parameters indicate that they are gravitationally bound. The IR and molecular line observations suggest, however, that they are in different evolutionary stages. AGAL329 harbors a strong 24 μm point source and show line profiles characteristics of infalling motions, indicating it is in a more advanced stage of evolution than AGAL333, which exhibits Gaussian profiles and no energy sources at IR wavelengths.

Table 2
Observational Parameters

SPW	Center Freq. (MHz)	Bandwidth (MHz)	Vel. res. (km s^{-1})
		Observing setup I	
N$_2$H$^+$	93173.402	117.19	0.393
CH$_3$CN	91985.284	117.19	0.398
Cont. 1	92500.000	1875.00	101.262
Cont. 2	103500.000	1875.00	90.500
Cont. 3	105400.000	1875.00	88.869
		Observing setup II	
HCO$^+$	89188.526	117.19	0.205
H^{13}CO$^+$	86754.288	117.19	0.211
Cont. 4	99000.000	1875.00	94.614
Cont. 5	100900.000	1875.00	92.832

3. Observations

We made ALMA Band 3 (86–116 GHz) dust continuum and molecular line observations toward the MDCs AGAL333 and AGAL329. Because the sizes of these MDCs are smaller than the ALMA field of view at 3 mm ($\sim$62$''$), single pointing observations were carried out, as part of Cycle 4, during 2016 December and 2017 January using both the 12 and 7 m ACA. We used two different spectral setups (see Table 2). In the first one, five separate spectral windows (SPWs) were used, three for continuum observations and two for observations of the N$_2$H$^+$ $J = 1 \rightarrow 0$ and CH$_3$CN $J = 5 \rightarrow 4$ lines. In the second setup, the bandwidth was separated into four SPWs, two for continuum observations and two for observations of the HCO$^+$ $J = 1 \rightarrow 0$ and H^{13}CO$^+$ $J = 1 \rightarrow 0$ lines. The observed molecular species were chosen for the following reasons: N$_2$H$^+$ suffers little depletion and is one of the best tracers of the dense and cold gas (Bergin & Langer 1997; Caselli et al. 2002). The emission in the HCO$^+$ and H^{13}CO$^+$ lines are, respectively, usually optically thick and thin toward dense clumps and therefore their simultaneous observations are useful to probe the presence of infall or expansion motions. The CH$_3$CN molecule is a good temperature probe, of both the large-scale

Table 3
Synthesized Beam and rms Noise from 7 m+12 m Combined Maps

Maps	AGAL329			AGAL333		
	rms noise (mJy/beam)	Beam ($'' \times ''$)	PA ($°$)	rms noise (mJy/beam)	Beam ($'' \times ''$)	PA ($°$)
Continuum	8.5×10^{-2}	1.5×1.3	155	4.7×10^{-2}	1.5×1.3	138
HCO^+	4.0	1.6×1.3	155	4.0	1.6×1.3	147
$H^{13}CO^+$	3.7	1.7×1.3	155	3.7	1.7×1.3	146
N_2H^+	4.0	2.1×1.7	66	4.0	2.1×1.7	67
CH_3CN	3.9	2.1×1.8	68	3.7	2.1×1.8	68

diffuse gas and small-scale dense gas (e.g., Güsten et al. 1985; Blake et al. 1987; Araya et al. 2005; Jones et al. 2008).

The integration time on source in each of the setups was 23 and 32 minutes for the 7 and 12 m array observations, respectively. The bandpass and flux calibrations were carried out using multiple quasars (J1603−4904, J1617−5848, J1427 −4206, J1603−4904, J1312−0424, J1617−5848, J1650 −5044, J1924−2914, J2131−1207), Mars and Callisto. Data calibration and reduction were made using the Common Astronomy Software Application (CASA; McMullin et al. 2007) version 4.7 package. Independently calibrated 12 and 7 m data sets were concatenated and cleaned together using the CASA *tclean* task with a Briggs weighting of 0.5. We used a *multi-scale* clean deconvolver (Cornwell 2008), with scale values of 0, 6, 10, and 30 times the image pixel size ($0.3''$). For the continuum imaging we concatenated all five continuum spectral windows. We used the interactive mode for continuum imaging while spectral cubes were made using continuum subtracted spectra with automated masking procedure *auto-multithresh* using the noise threshold parameter *noisethreshold* of 2 sigma. This parameter corresponds to the minimum signal-to-noise value that is masked. This technique mimics what we would do in manual masking in interactive cleaning procedure. From the final spectral line cubes, integrated intensity, and velocity maps were made using CASA task *immoments*. The angular resolution achieved in the continuum observations are $1.46'' \times 1.34''$ (P.A. $155°$) and $1.46'' \times 1.33''$ (P.A. $138°$) for AGAL329 and AGAL333, respectively. The root mean square values of the noise achieved in the continuum and line maps are listed in the Table 3. For the molecular lines the root mean square noise reported is that determined from line-free channels.

4. Results

4.1. Continuum Emission

Figure 3 shows our ALMA images of the 3 mm continuum emission toward AGAL329 and AGAL333. The emission from AGAL329 arises from an extended, bright central source and a handful of compact, weaker structures. The emission from AGAL333 arises from several compact structures spread out across the region, most of them being aligned in a NE–SW direction.

In order to be quantitative in the identification of structures in the images we used two commonly employed methods: *Astro-dendro*[7] and *Clumpfind* (Williams et al. 1994). We note that, in general, the number of extracted features and their parameters depend on the applied method (e.g., Pineda et al. 2009).

_____

To identify structures in the *Astrodendro* algorithm, based on a dendrogram analysis (Rosolowsky et al. 2008), requires three inputs parameters: the minimum flux to be considered (F_{min}), the separation between neighboring peaks (δ) and the minimum number of pixels (A_{min}) a structure should have. For a robust extraction of structures we adopted $F_{min} = 3\sigma$, $\delta = 1\sigma$, and $A_{min} = 1$ beam. The key characteristic of this algorithm is its ability to track hierarchical structures over a range of scales. The *Clumpfind* algorithm (Williams et al. 1994) is based on contouring the data array at different levels. The three input parameters are: the minimum flux level to be considered (T_{low}), the contour step (ΔT) and the minimum number of pixels (S_{min}) required to be defined as a unique substructure. For core extraction we adopted $T_{low} = 3\sigma$, $\Delta T = 2\sigma$ and $S_{min} = 1$ beam.

Toward AGAL329, Astrodendro identified nine cores while *Clumpfind* recovered 10. Toward AGAL333, Astrodendro identified 11 cores while Clumpfind identified 10 cores. The list of cores and their observed parameters are presented in Table 4. Columns 2 and 3 give the peak position, Columns 4 and 5 give, respectively, the flux densities and deconvolved angular sizes (half-width at half-maximum (HWHM)) determined from *Clumpfind* and Columns 6 and 7 those determined using *Dendrogram*. We find that the flux densities and angular sizes of the structures (cores) obtained from both methods are similar. Given the similarities, in the remaining of this paper we will use the parameters of the cores determined from the *Clumpfind* method (labeled in Figure 3).

4.2. Molecular Line Emission

Molecular line emission was detected in all four observed species toward both MDCs. We note that the spectrum of the $J = 1 \rightarrow 0$ transition of N_2H^+ consists of seven hyperfine (HF) components (Caselli et al. 1995), however, due to the overlap of closely spaced HF components, and only three distinct lines are observed. This is illustrated in Figure 4, which shows the N_2H^+ spectrum observed toward core mm-4 in AGAL333. The lower velocity component of these three lines, centered at the frequency of 93176.265 MHz, corresponds to a single HF component, whereas the other two lines are blends of HF components. Also shown in Figure 4 is the spectrum of the rotational $J = 5 \rightarrow 4$ transition of CH_3CN observed toward core mm-6 in AGAL329. This rotational transition consists of 5 K components (marked in red), with K being the projection of the total angular momentum of the molecule about the principal rotation axis of the molecule. Their line frequencies, upper state energy levels, and line strengths are given in Table 5.

To describe the emission at each position within the MDCs we performed moment analysis of the data (Sault et al. 1995), computing the zeroth (integrated intensity), first (intensity
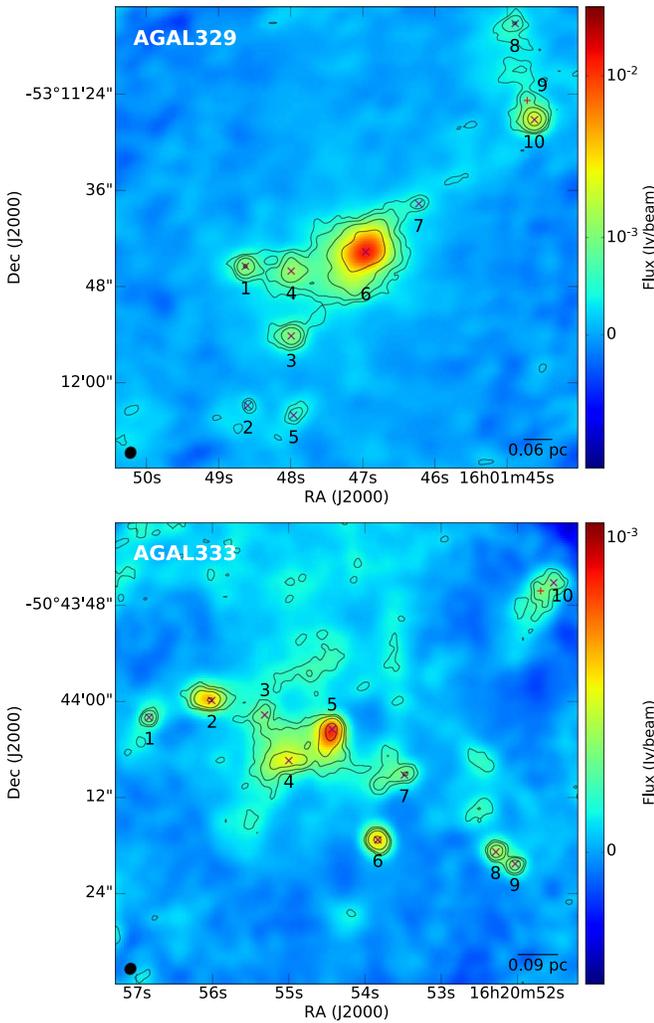
Figure 3. Images of the 3 mm continuum emission observed with ALMA toward the protostellar clump AGAL329 (upper panel) and prestellar clump AGAL333 (lower panel). The magenta crosses indicate the cores extracted in common by *Astrodendro* and *Clumpfind*. The "+" symbols in red indicate cores identified only by *Clumpfind* or *Astrodendro*. The scale bar in the bottom right corner indicates the Jeans radius of the clumps. Also shown are contour levels of the 3 mm emission, drawn at 3σ, 5σ, 10σ, and 30σ, where σ are 4.7×10^{-2} and 8.5×10^{-2} mJy/beam for AGAL333 and AGAL329, respectively. The black ellipse shown at the bottom left corner indicates the beam size.

weighted velocity field), and second (intensity weighted velocity dispersion) moments. This approach allows an easy comparison of the characteristics of the emission in the different molecular transitions. The moments of the N_2H^+ emission were computed using the lower velocity component of the three observed lines because it corresponds to a single HF component. To make moment maps of the CH_3CN $J = 5 \rightarrow 4$ emission toward AGAL329 we used the emission observed in the $K = 2$ component, which is the stronger unblended component. Emission in this line was not detected toward AGAL333 and therefore we used the emission in the $5_0 \rightarrow 4_0$ component for the moment analysis.

4.2.1. Morphology

AGAL329: Figure 5 show images of the velocity integrated line emission (moment 0) in all four observed species toward

AGAL329. The peak position of the continuum cores are marked with crosses. The velocity range of integration is from -84.0 to -32.0 km s^{-1} for HCO^+, -64.0 to -40.0 km s^{-1} for $H^{13}CO^+$, from -64.0 to -54.0 km s^{-1} for N_2H^+ (corresponding to the lower velocity component of the HF structure), and from -41.0 to -23.0 km s^{-1} for the CH_3CN corresponding to the $J_K = 5_2 \rightarrow 4_2$ component. The morphology of the line emission is noticeably different in the four transitions, most likely due to differences in optical depths, excitation conditions, and chemistry.

The emission in the N_2H^+ line (upper left panel) is the brightest and most extended one of the four observed species. It exhibits a bright central region, with a radius of $\sim6''$, surrounded by weaker emission from a region of $\sim20''$ in radius, and an extended region of emission seen toward the northwest of the image (labeled northwest), which is associated with the GLIMPSE source G329.1845-00.3045 (Robitaille et al. 2008). The bright central region exhibits a clumpy ring-like structure with three distinct condensations. The two westernmost condensations are associated with the mm-6 core, but their peak positions do not agree with the peak position of the continuum source, and the easternmost condensation is associated with the mm-4 core. All continuum cores are associated with N_2H^+ emission. A conspicuous feature of the N_2H^+ image, is a region $\sim15''$ north of the central cores (labeled north), with a size of $\sim11''$ in diameter, which is not present in the other images and does not harbor continuum sources. Figure 6 presents a *Spitzer* image of the $8\,\mu m$ emission toward AGAL329, which clearly shows that this MDC is associated with an infrared dark cloud, superimposed with contours of the N_2H^+ emission. The morphology of the latter closely follows the $8\,\mu m$ dark features, indicating that N_2H^+ is tracing gas with high column densities. Interestingly the north N_2H^+ region is well correlated with an $8\,\mu m$ dark feature. This, together with lack of emission in the HCO^+, $H^{13}CO^+$, and CH_3CN lines suggests that this region is composed of dense and cold gas that has undergone high levels of depletion.

The morphology of the HCO^+ emission exhibits noticeable differences with respect to that of the N_2H^+ emission. Toward the central N_2H^+ region, the HCO^+ emission shows a banana-like morphology, which is roughly coincident with the two westernmost N_2H^+ condensations, but no HCO^+ emission is seen from the eastern N_2H^+ condensation. The peak position of the mm-6 core is located at the western edge of the banana. Toward the extended northwest region, the brighter HCO^+ emission is seen at its northern end (core mm-8), while the brighter N_2H^+ emission is seen at its southern end (core mm-10). In addition, the HCO^+ image shows two conspicuous features: a bright clumpy structure, located $\sim18''$ south of the central region, elongated in the NE–SW direction (labeled south), barely seen in N_2H^+, and a weak V-shaped feature located $\sim10''$ west from the central region (labeled west), not seen in the N_2H^+ image.

The $H^{13}CO^+$ emission exhibits a bright central component, with a size of $5.5''$, which encompasses mm-6, diffuse emission seen toward the east, similar in extent to that seen in N_2H^+, and emission from the northwest region.

The most prominent features in the CH_3CN image are a bright central region, with a size of $6''$, whose peak position coincides with the peak position of core mm-6, a bright V-shaped region coincident with the west region seen in HCO^+

Table 4
Observed Parameters of the Cores

| Core | Peak Position | | Clumpfind | | Astrodendro | |
	R.A. hh:mm:ss	Decl. dd:mm:ss	Flux (mJy)	Ang. Size (HWHM ″)	Flux (mJy)	Ang. Size (HWHM ″)
			AGAL329			
mm-1	16:01:48.62	−53:11:45.47	4.69	0.65	3.78	0.65
mm-2	16:01:48.59	−53:12:02.87	0.49	0.29	0.50	0.41
mm-3	16:01:47.99	−53:11:54.17	5.12	0.75	5.17	1.09
mm-4	16:01:47.99	−53:11:46.07	9.84	1.14	5.60	0.84
mm-5	16:01:47.95	−53:12:04.07	1.04	0.50	1.05	0.61
mm-6	16:01:46.95	−53:11:43.67	102.15	1.77	93.55	1.66
mm-7	16:01:46.22	−53:11:37.67	1.00	0.51	0.61	0.45
mm-8	16:01:44.88	−53:11:15.17	2.48	0.77	2.50	1.06
mm-9[a]	16:01:44.72	−53:11:24.77	2.74	1.24	…	…
mm-10	16:01:44.62	−53:11:27.17	8.88	0.67	11.74	1.42
			AGAL333			
mm-1	16:20:56.83	−50:44:01.98	0.32	0.31	0.33	0.43
mm-2	16:20:56.01	−50:43:59.88	1.77	0.61	1.81	0.74
mm-3	16:20:55.31	−50:44:01.69	0.46	0.53	0.31	0.50
mm-4	16:20:54.99	−50:44:07.39	3.12	1.22	2.44	1.23
mm-5	16:20:54.43	−50:44:03.49	4.25	0.91	3.76	0.97
mm-6	16:20:53.83	−50:44:17.29	1.38	0.50	1.41	0.60
mm-7	16:20:53.48	−50:44:09.19	0.58	0.78	0.60	0.77
mm-8	16:20:52.28	−50:44:18.78	0.57	0.39	0.59	0.50
mm-9	16:20:52.02	−50:44:20.28	0.42	0.34	0.43	0.45
mm-10	16:20:51.52	−50:43:45.18	0.68	0.87	0.22	0.45
mm-11[b]	16:20:51.71	−50:43:46.62	…	…	0.25	0.43

Notes.
[a] Core not detected by *Astrodendro*.
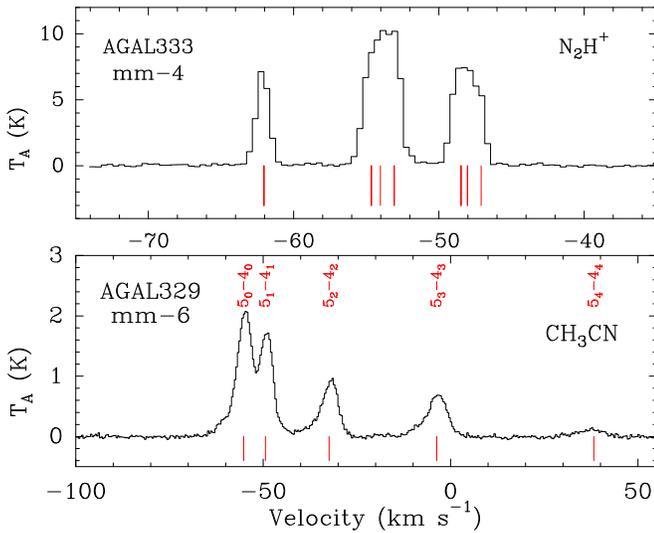[b] Core not detected by *Clumpfind*.

Figure 4. Top panel: $N_2H^+ (J = 1 \rightarrow 0)$ spectrum from core mm-4 in AGAL333. The red vertical lines at the bottom mark the velocities of the seven HF components. Bottom panel: $CH_3CN (J = 5 \rightarrow 4)$ spectrum from core mm-6 in AGAL329. The red vertical lines at the bottom mark the velocities of the five K components, labeled at the top.

and an elongated, clumpy structure of weak emission running from northwest to southeast, which is closely associated with dark lanes seen in the 8 μm *Spitzer* images. We note here that the moment zero map of the CH_3CN emission was made using the emission in the $K = 2$ component in AGAL329 in order to

Table 5
$CH_3CN J = 5 \rightarrow 4$ Rotational Lines

Transition	Frequency (MHz)	Velocity Shift[a] (km s^{-1})	Eu/k (K)	Strength $(J^2 - K^2)/J$	$S(I,K)$ $g_k g_I$
$5_0 \rightarrow 4_0$	91987.09	…	13.2	5.0	1/2
$5_1 \rightarrow 4_1$	91985.31	5.79	20.4	4.8	1/2
$5_2 \rightarrow 4_2$	91979.99	23.14	41.8	4.2	1/2
$5_3 \rightarrow 4_3$	91971.13	52.04	77.5	3.2	1
$5_4 \rightarrow 4_4$	91958.73	92.50	127.6	1.8	1/2

Note.
[a] Shift with respect to the $5_0 \rightarrow 4_0$ line.

avoid blending effects. The emission in the lower K components is much brighter and extended than in the higher K components.

Figure 5 also shows clear differences in the strength of emission from the cores in the different lines, likely caused by differences in optical depths, excitation conditions, and/or chemistry. The differences are illustrated by considering the three cores located in the northwest region of the clump: core mm-8 shows bright emission in HCO^+ and $H^{13}CO^+$, core mm-10 is brighter in N_2H^+ and CH_3CN, while core mm-9 is brighter in HCO^+.

AGAL333: Figure 7 presents images of the velocity integrated emission (moment 0) in all four observed species toward AGAL333, showing that the morphology of
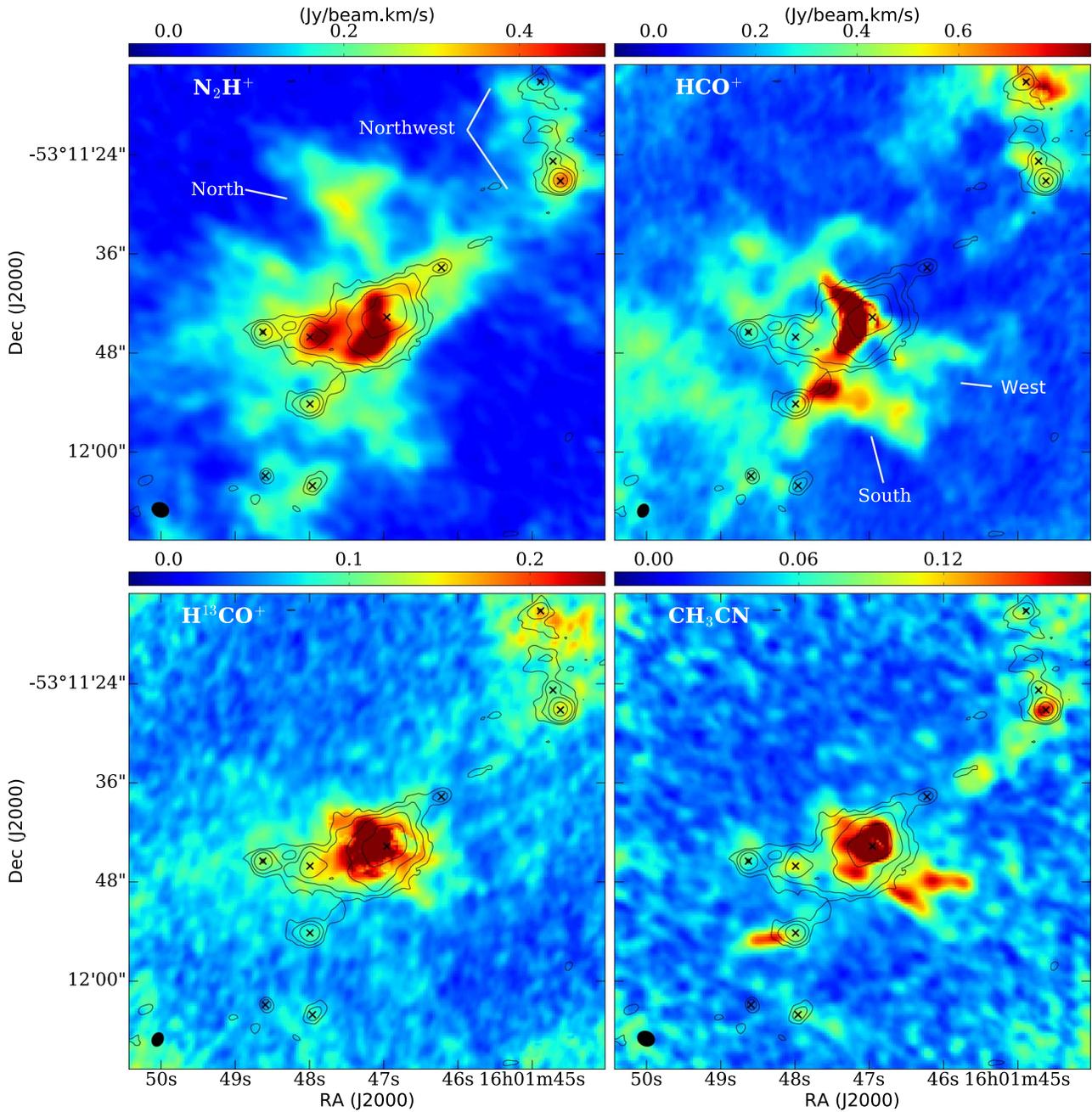
6

Figure 5. Images of the velocity integrated line emission toward AGAL329. Superimposed are contours of the continuum emission. Black crosses mark the peak position of the continuum cores. The black ellipse shown at the bottom left corner indicates the beam size. Top left: N_2H^+; top right: HCO^+, bottom left: $H^{13}CO^+$, bottom right: CH_3CN. Labeled in the different panels are conspicuous features discussed in the text.

the line emission is different in the four molecules. The peak position of the continuum cores are marked with crosses. The velocity range of integration is -60.0 to -48.0 km s^{-1} for HCO^+ and $H^{13}CO^+$, -67.0 to -60.0 km s^{-1} for N_2H^+ and from -64.0 to -57.0 km s^{-1} for the CH_3CN corresponding to the $J_K = 5_0 \rightarrow 4_0$ component. The emission in N_2H^+ line is the brightest and most extended one, delineating a complex network of filamentary structures across the whole region. The main structure is a clumpy filament running from northeast to southwest, P.A. of 60°. All of the continuum cores are associated with N_2H^+ emission and most of them lie within the main filament. There is a high degree of correlation between the N_2H^+ and the continuum emissions.

The HCO^+ emission (upper right panel) clearly delineates the main filament running from northeast to southwest. The brighter peaks of the HCO^+ emission are associated with cores mm-2 and mm-3. The morphology of the $H^{13}CO^+$ emission shows some similarities to that of N_2H^+, exhibiting a network of filamentary structures. However, the peak position of the brighter $H^{13}CO^+$ structures do not coincide with those of the continuum cores. In fact there is an anticorrelation between the $H^{13}CO^+$ and continuum emissions. The brighter feature in both the $H^{13}CO^+$ and N_2H^+ images corresponds to a region in between cores mm-3 and mm-4. Finally, emission in the CH_3CN line (lower right panel) was clearly detected only toward core mm-2 core and weakly detected toward cores mm-1, mm-3, mm-4, and mm-5.
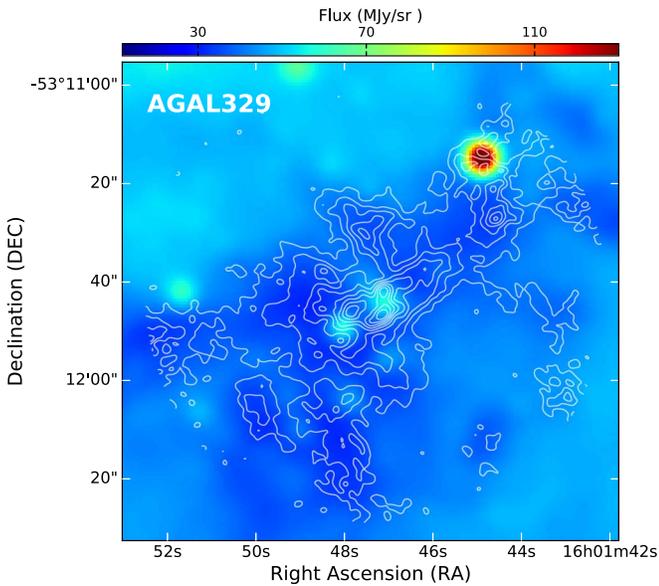
Figure 6. *Spitzer* 8 μm image toward AGAL329 overlaid with contours of the velocity integrated N₂H⁺ emission observed with ALMA. Contour levels are drawn from 10%–90% of the peak emission of 0.70 Jy beam⁻¹ km s⁻¹, with a step of 10%.

4.2.2. Velocity Field

In order to investigate the velocity field across the MDCs we consider the emission in the N_2H^+ line, which is bright and optically thin and therefore less affected by self-absorption effects. Figure 8 shows images of the velocity field (moment 1) of the N_2H^+ emission toward AGAL329 and AGAL333.

Figure 8 (right panel) shows that there is a significant velocity gradient from northeast to southwest across AGAL333. There is a velocity shift of 4.2 km s⁻¹ over a region of about 50″, which at the distance of 3.72 kpc corresponds to a velocity gradient of 4.7 km s⁻¹ pc⁻¹. Assuming that the velocity gradient is due to gravitationally bound rotation of an structure with radius R and mass M, then $M = (dV/dR)^2 R^3/G$ (see, Armstrong et al. 1985). The observed velocity gradient implies a mass within a radius of 0.45 pc of 460 $M_\odot$. This mass is within a factor of 2 from the mass derived from the dust observations, giving support to the bound rotation hypothesis.

The velocity field toward the protostellar clump (Figure 8, left panel) appears complex, with no organized motions nor clear velocity gradients seen across the clump. The redder velocities seen toward the north and the bluer velocities seen toward the south are probably caused by the presence of outflows, as discussed next. In several positions across this clump the profiles of the HCO^+ line emission exhibit the presence of wing emission. To investigate the spatial distribution of the wing emission, we made contour maps of the velocity integrated emission in three ranges of radial flow velocities. The radial flow velocity, v_{flow}, is defined as $v_{LSR} - v_0$, where v_0 is the systemic velocity of the clump, assumed to be -50.5 km s⁻¹. Figure 9 shows maps of the wing emission, overlaid on the ALMA dust continuum image, in three ranges of flow velocities: $20 < |v_{flow}| < 35$ km s⁻¹, referred as the high velocity (HV) wing, $12 < |v_{flow}| < 20$ km s⁻¹, referred as the intermediate velocity (IV) wing, and $5 < |v_{flow}| < 12$ km s⁻¹, referred as the low velocity (LV) wing. The morphology of the HCO^+ wing emission is complex.

Clearly distinguished in the LV map is an extended bipolar-like structure with a wide opening angle (half opening angle of ~43°), consisting of a lobe of redshifted emission seen toward the north and a lobe of blueshifted emission seen toward the south, located on opposite directions from core mm-6. The position angle of the symmetry axis of the outflow is P.A. ~5°. The linear extensions of the redshifted and blueshifted lobes along the symmetry axis are ~0.23 pc (~14″) and ~0.27 pc (~16″), respectively. Also distinguished in the LV map is a second, more collimated, bipolar-like structure, with a position angle of 45°, consisting of a redshifted lobe extending toward the southwest and a blueshifted lobe extending toward the northeast from core mm-6. The blueshifted lobe extends ~0.12 pc (~7″) northeast while the redshifted lobe extends ~0.25 pc (~15″) southwest. In addition, seen in the LV map is a weak blueshifted feature extending toward the northeast and a weak redshifted feature extending toward the southeast from core mm-10. These features may correspond to streams of gas infalling toward core mm-10.

In the IV map, emission from the wide angle bipolar structure is only seen from the blueshifted lobe. In this velocity range emission from the more collimated bipolar structure is clearly seen at redshifted velocities. In the HV map, the blueshifted emission associated with the mm-core 6 is compact (~3″), while the redshifted emission extending west shows three separate "knot" like features, at distances of ~3″, ~6.5″, and ~10″ from the peak position of mm-6. It is notable that this emission region is also detected in CH_3CN emission (see Figure 5, labeled west). Also seen in the HV map is a narrow blueshifted emission, of size ~4″, associated with mm-3.

4.3. Line Emission from Cores

In this section we present the characteristics of the spectra of the molecular line emission from the continuum cores. The spectra correspond to the average spectra of the spatially integrated emission over the solid angle subtended by each core (hereafter referred to as the core spectra).

Figure 10 shows the spectra of the N_2H^+ $J = 1 \rightarrow 0$ line. Emission is clearly detected toward all cores in both MDCs. The red line shows the result of a simultaneous fit to the emission from the whole HF structure for a single velocity component, made using the task *pyspeckit.models* in the *PySpecKit* (Ginsburg & Mirocha 2011). This approach gave good results for all cores in AGAL333 and for most cores in AGAL329, except cores mm-3, mm-4, and mm-6, which exhibit either self-absorption profiles or strong wing emission. Thus, for cores mm-3 and mm-4 in AGAL329 we fitted a single Gaussian profile to the lower velocity (single HF) component (green line), while for core mm-6, two velocity components were used to fit the spectra.

Figure 11 shows, in the same panel, the spectra of the HCO^+ (black line) and $H^{13}CO^+$ (red line) emission. Emission in these lines was detected from all cores in both MDCs, except toward core mm-9 in AGAL333 in which the $H^{13}CO^+$ line was not detected (<3σ). The HCO^+ profiles from several cores in AGAL329 display line asymmetries and self-absorption features. Typically the HCO^+ profile shows two peaks with a strong blueshifted peak and weak redshifted peak relative to the velocity of the optically thin $H^{13}CO^+$ line. This is a characteristic signature of infalling gas, probably due to the global collapse of the clump (see Section 5.4).
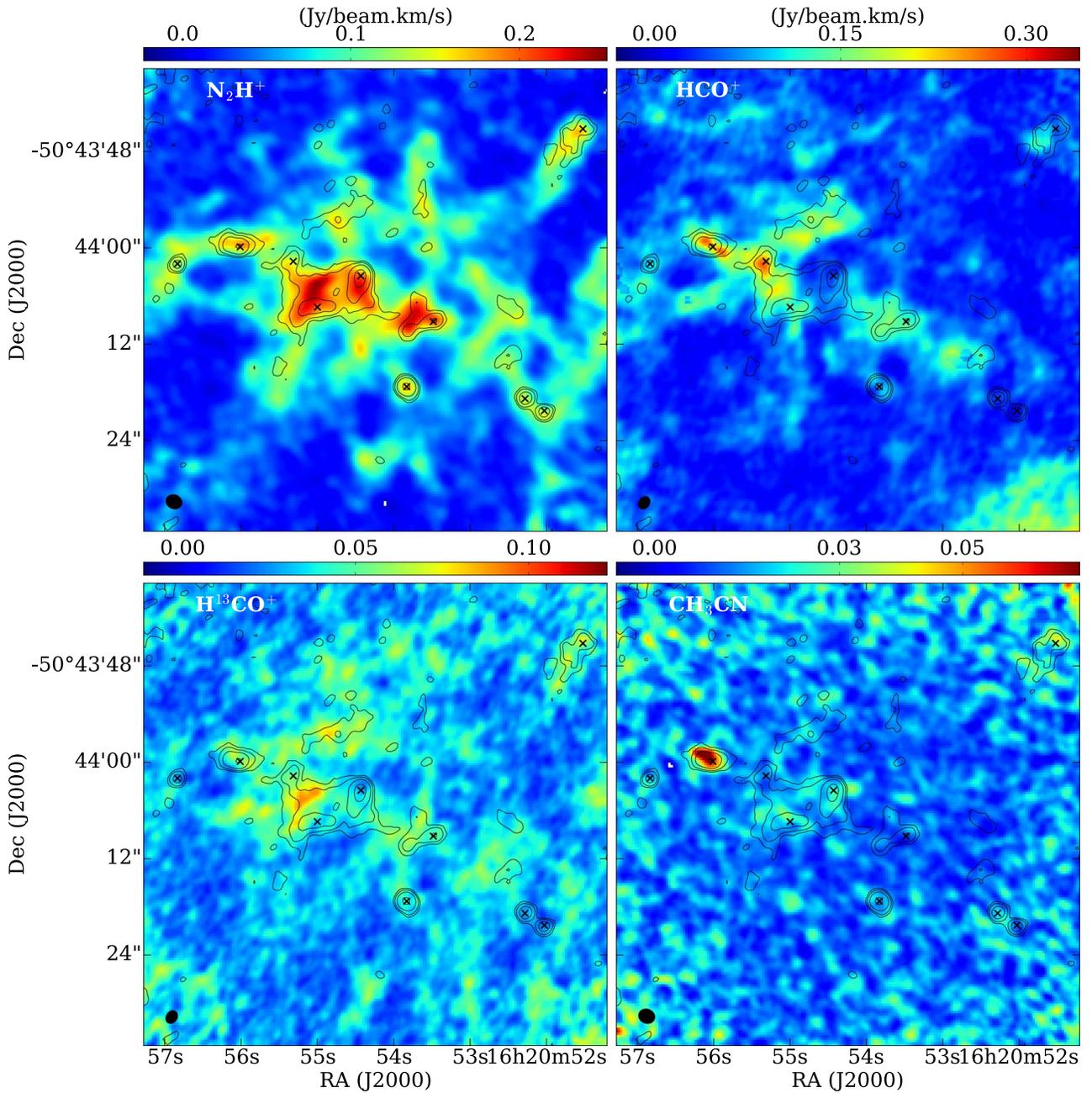
Figure 7. Images of the velocity integrated line emission toward AGAL333. Superimposed are contours of the continuum emission. Black crosses mark the peak position of the continuum cores. The black ellipse shown at the bottom left corner indicates the beam size. Top left: N_2H^+; top right: HCO^+, bottom left: $H^{13}CO^+$, bottom right: CH_3CN.

Most cores within the AGAL333 prestellar clump show absorption features and/or shoulders in the HCO^+ line. Cores mm-1, mm-2, mm-4, mm-5, and mm-10 show inverse P Cygni profiles, suggesting that they are undergoing contraction motions. On the other hand cores mm-6, mm-7, and mm-8 show P Cygni–like profiles, usually taken as a signpost of outflowing or expanding gas motions. It is possible that some of the cores formed in MDCs are transient objects and therefore are expanding. In fact the mm-7 core has a virial parameter of 2.5, further suggesting it is not bounded.

Figure 12 presents the observed spectra in the $J_K = 5_K \rightarrow 4_K$ CH_3CN K-ladder. Emission was detected from all cores within AGAL329, except mm-2. Emission was detected in all five K components toward one core (mm-6), in four K components

toward five cores (mm-1, mm-3, mm-4, mm-7, and mm-10), in three K components toward two cores (mm-5 and mm-9), and in two K components toward one core (mm-8). Toward AGAL333, only weak CH_3CN emission was detected from cores mm-1, mm-2, mm-3, mm-4, and mm-5.

4.3.1. Line Parameters of Optically Thin Transitions

The determination of the kinematics (velocities), turbulence (line widths), and dynamical state of the cores (virial parameter) requires observations of the emission in optically thin molecular lines, because they are free of self-absorption features. Table 6 lists the parameters of the core emission in the optically thin $J = 1 \rightarrow 0$ lines of $H^{13}CO^+$ and N_2H^+.
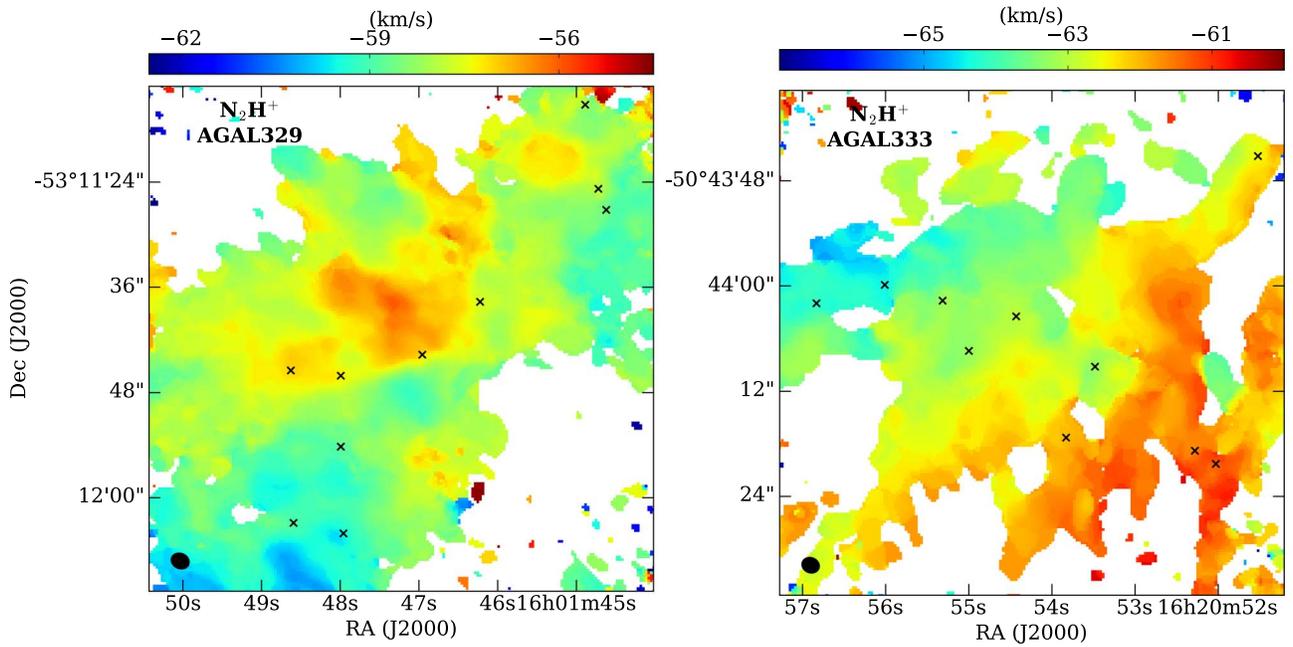
Figure 8. Moment 1 images of the N_2H^+ emission from AGAL329 (left) and AGAL333 (right). Crosses mark the peak position of the continuum cores.
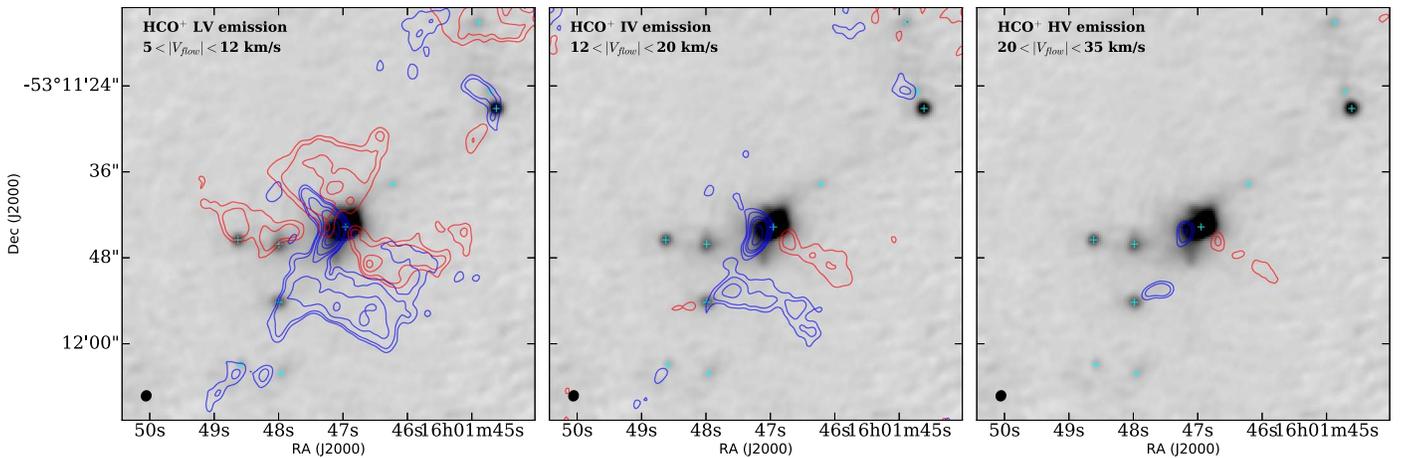

Figure 9. Contour maps of LV, IV, and HV HCO^+ emission toward AGAL329 overlaid in the 3 mm ALMA continuum map (gray scale). The blue and red color contours mark blueshifted and redshifted emission, respectively. The flow velocity range is shown in the top left corner of each map.

The former were determined from a Gaussian fit to the core spectra, while the latter were derived in most cases from a simultaneous fit to all HF lines. For core mm-6 in AGAL329 two velocity components were used to fit the N_2H^+ and $H^{13}CO^+$ profiles. In addition to the central velocity and line width, the simultaneous HF fit provides the total optical depth in the N_2H^+ $J = 1 \rightarrow 0$ transition. The derived total optical depths range from ~1.4–12.5 for the cores in prestellar source and from ~0.5–10.1 for the cores in the protostellar source. Even though the total optical depths are $\geqslant 1$, the individual HF components are mostly optically thin. As shown in Figure 13, the velocities and line widths of the cores derived from both lines are in good agreement.

In general the line widths of the cores in the prestellar clump are smaller than those of the cores in the protostellar clump (see Figure 13). The average line width of the cores within AGAL333 and AGAL329 are 1.2 and 2.0 km s^{-1}, respectively. The explanation of the large line widths in cores within the protostellar clump is not straightforward, and it may reflect

either an increase in the level of turbulence due to the beginning of star formation activity or an increase in the gas velocities due to collapse motions. In particular, Vázquez-Semadeni et al. (2009) concluded that in a cloud undergoing global gravitational collapse, the velocity dispersion at all scales are caused by infall motions rather than by turbulence.

5. Analysis and Discussion

In this section we discuss the physical parameters of the cores, their spatial distribution, virial state, and the fraction of the total mass in cores relative to the parent clump mass, all of which are key properties to discern among the different models of fragmentation of MDCs.

5.1. Core Parameters

The physical parameters of the cores are listed in Table 7 and their derivation is discussed in what follows.
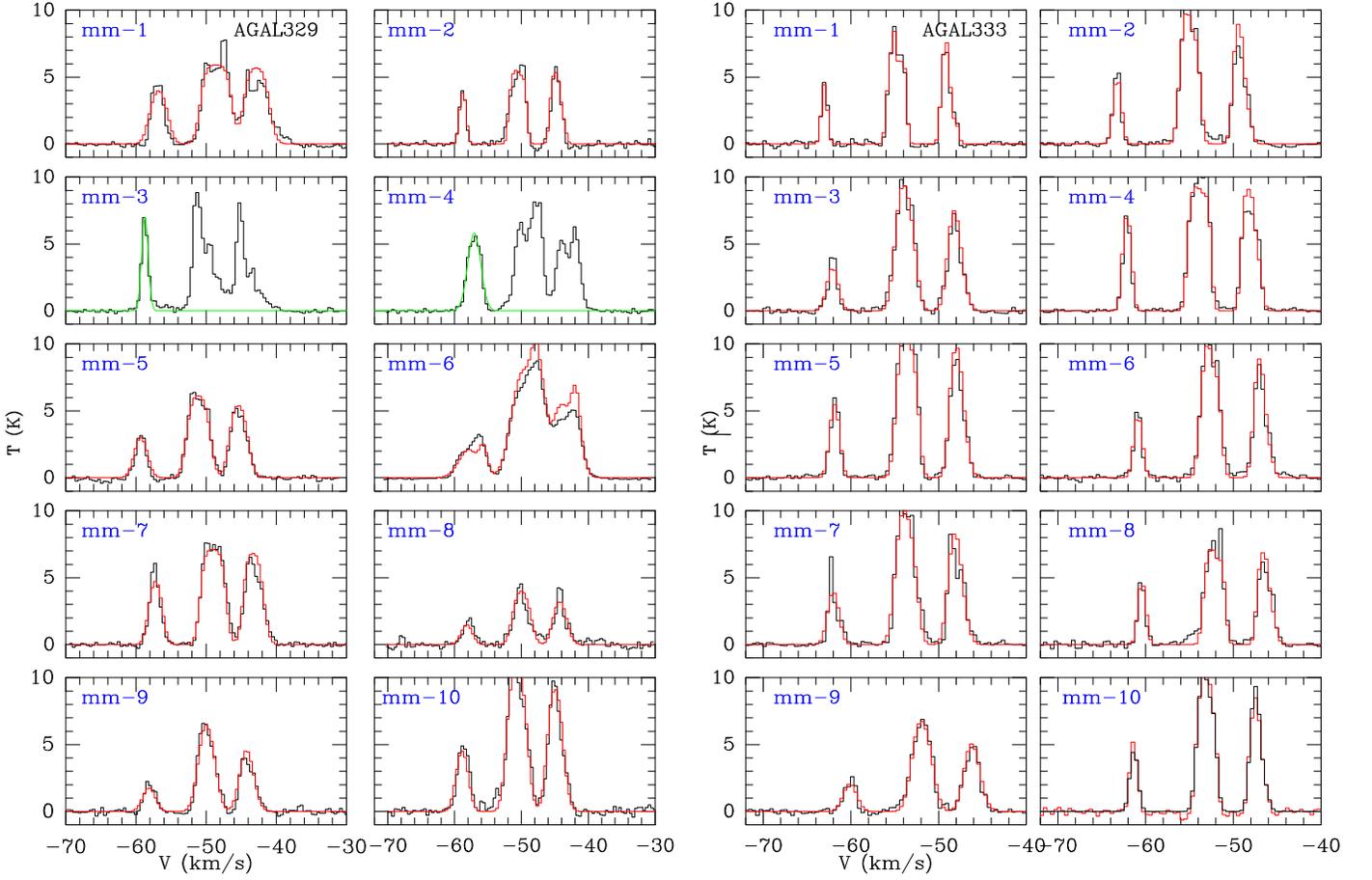
Figure 10. Average spectra of the N_2H^+ emission from cores. Left panel: AGAL329 cores. Right panel: AGAL333 cores. The red line indicates the result of a simultaneous fit to the whole HF structure and the green line indicates the result of a Gaussian fit to the lower velocity component.

5.1.1. Sizes

The radius of the cores were computed from the geometric mean of the semimajor and minor axis determined from *Clumpfind* and the distances given in Table 1. For cores in AGAL329 the radii range from 0.005–0.030 pc (1000–6200 au) with an average value of 0.014 pc (2900 au), while for cores in AGAL333 the radii range from 0.006–0.022 pc (1200–4500 au) with an average value of 0.012 pc (2500 au).

5.1.2. Temperatures

The detection of emission in at least two $J = 5_K \to 4_K$ transitions of CH_3CN allows determining the rotational temperature of methyl cyanide, which is known to provide a good estimate of the kinetic temperature of the gas (e.g., Güsten et al. 1985; Remijan et al. 2004; Hernández-Hernández et al. 2014). We use the standard rotational diagram analysis (Turner 1991; Sutton et al. 1995), which assumes that the lines are optically thin and that the population levels are characterized by a single excitation temperature (LTE assumption). Integration of the transfer equation of the emission in a line with an upper energy level, E_u, leads to the expression (e.g., Blake et al. 1987; Araya et al. 2005),

$$\ln\left[\frac{3c^2}{16\pi^3\Omega_s\nu^3}\frac{J}{\mu^2 S(I,\ K)(J^2 - K^2)}\int S_\nu dv\right]$$
$$= \ln\left[\frac{N_t}{Q(T_{\rm rot})}\right] - \left[\frac{E_u}{kT_{\rm rot}}\right], \qquad (3)$$

where $\int S_\nu dv$ is the velocity integrated flux density of the line, Ω_s the solid angle subtended by the source, $S(I,\ K)$ the degeneracy due to spin, ν and μ the transition frequency and dipole moment of the molecule, respectively, $T_{\rm rot}$ the rotational temperature, $Q(T_{\rm rot})$ the rotational partition function, and N_t is the total column density. The dipole moment of CH_3CN molecule is 3.91 debye and the spin degeneracies for the $J = 5 \to 4$ transitions are given in Table 5.

Rotational diagrams for AGAL329 and AGAL333 cores, for which at least three lines in the 5_K–4_K K-ladder were detected above the 3σ level, are shown in Figures 14 and 15, respectively. The velocity integrated flux density, obtained by integrating the flux per beam over a circular region with angular radius given in Column 7 of Table 8, are given in Columns 2–6 for $K = 0$, 1, 2, 3, and 4 lines, respectively. From a least squares fit to the data we derived the rotational temperatures given in Column 8 of Table 8. Clearly, the cores within the protostellar clump are warmer than in the prestellar clump. The temperature of cores within the protostellar clump range from 28–68 K, with an average value of ~38 K. Within the prestellar clump only three cores (mm-2, mm-4, and mm-5) were detected in at least three 5_K–4_K lines, for which we derived temperatures of 31, 30, and 24 K, respectively. Whether the source of heating of the cores in the protostellar clump is due to the presence of embedded protostellar activity or from their gravitational collapse remains to be investigated.
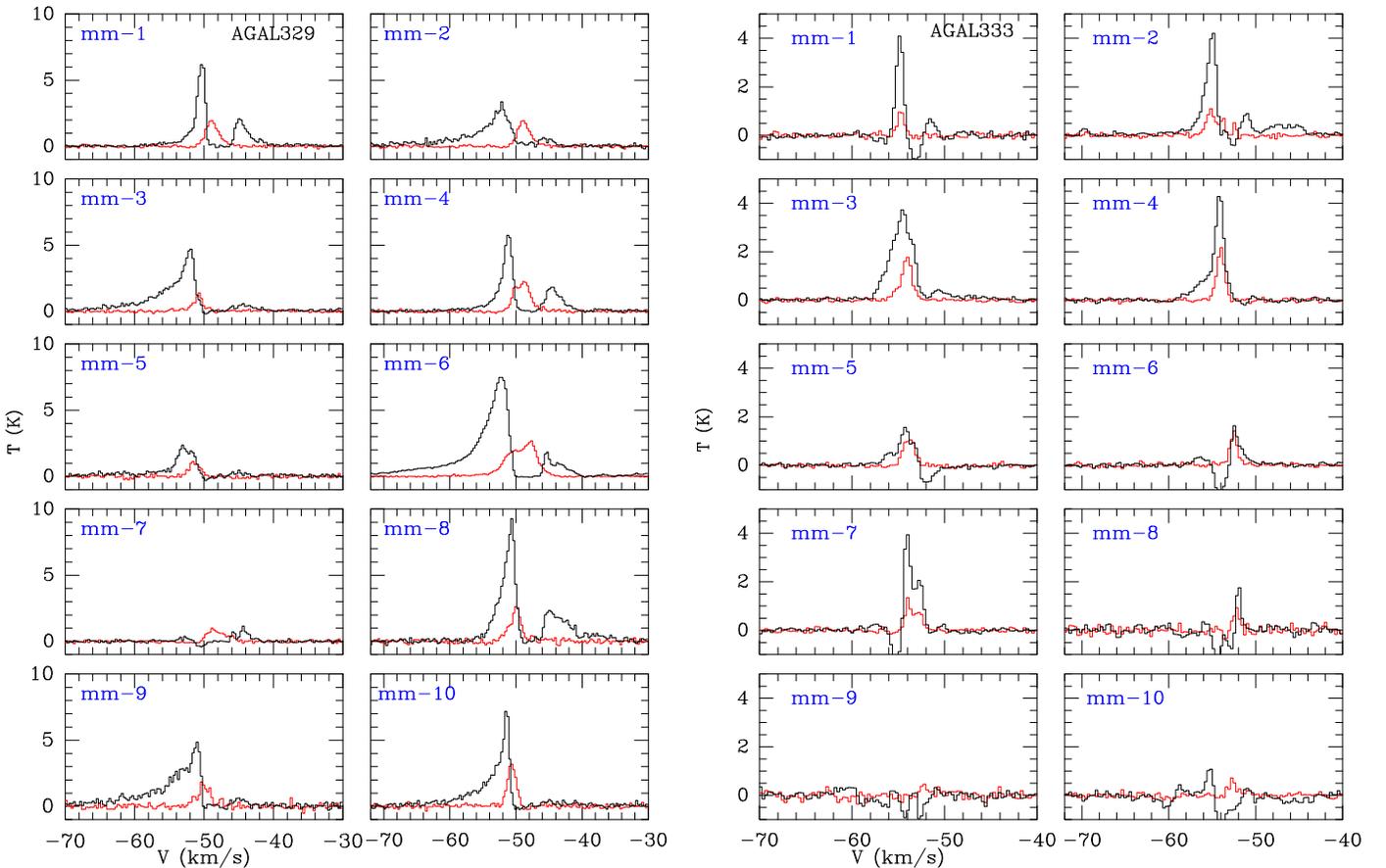
Figure 11. Average spectra of the HCO$^+$ (black line) and H^{13}CO$^+$ (red line) emission from cores. Left: AGAL329 cores. Right: AGAL333 cores.

The fit also gives the value of $\frac{N_t}{Q(T_{rot})}$, which allows deriving the CH$_3$CN column density. Using the following expression for the partition function of CH$_3$CN (Araya et al. 2005),

$$Q(T_{rot}) = 3.89 \frac{T_{rot}^{1.5}}{(1 - e^{-524.8/T_{rot}})^2}, \tag{4}$$

and the rotational temperatures of the cores, the derived CH$_3$CN column densities are given in Column 9 of Table 8. The cores in the protostellar clump have column densities ranging from 2.4×10^{14} to 3.2×10^{15} cm^{-2}, while the mm-2, mm-4, and mm-5 cores in the prestellar clump have column densities of 1.1×10^{14}, 5.1×10^{13}, and 5.0×10^{13} cm^{-2}, respectively.

It is worth mentioning that one of the assumptions of the rotational diagram method applied above, namely, that lines should be optically thin, is well fulfilled by the emission in the $J = 5_K \rightarrow 4_K$ lines from all cores. For instance, for core mm-6 in AGAL329, the most extreme case because it exhibits the largest column density, the optical depths in the CH$_3$CN $J = 5_K \rightarrow 4_K$, $K = 0, 1, 2, 3, 4$ lines are 0.23, 0.19, 0.11, 0.04, and 0.02, respectively. If we use the more general rotational diagram method that takes into account optical depth effects (see, Goldsmith & Langer 1999), the differences in the derived temperatures and column densities are well within the errors determined from the "traditional" approach.

Due to the large spatial extent of the CH$_3$CN emission from the central region of AGAL329, whose peak position coincides with the peak position of core mm-6, it was possible to determine the dependence of the rotational temperature with the radius. Figure 16 (left panel) shows rotational diagrams of the CH$_3$CN emission integrated over six different regions: from top to bottom, an inner disk with a radius of $1''$ and five circular annuli with inner radii from $1''$ to $5''$ and widths of $1''$. The derived rotational temperature and column densities are given in Columns 8 and 9 of Table 9, respectively. The rotational temperature decreases from 131 ± 24 K at the peak position to 30 ± 3 K at a radial distance of $6''$ from the center. Also shown in the middle and right panels of Figure 16 are, respectively, the rotational temperature and CH$_3$CN column density dependence with radius. Power-law fits to the rotational temperature profile ($T_{rot} \propto r^q$) and column density profile ($N \propto r^s$) give power-law indices of -0.8 ± 0.2 and -2.0 ± 0.4, respectively.

5.1.3. Masses

The mass of the cores were calculated from the continuum flux density, S_ν, using the expression,

$$M = \frac{S_\nu D^2 R_{gd}}{k_\nu B(T, \nu)}, \tag{5}$$

where k_ν is the dust mass absorption coefficient at frequency ν, $B(T,\nu)$ is the Planck function at temperature T, D is the distance, and R_{gd} is the gas-to-dust ratio. We assume $R_{gd} = 100$ and $k_{100\,GHz} = 0.21$ cm^2 g^{-1} corresponding to the dust grains with ice mantles at gas densities of 10^6 cm^{-3} (Ossenkopf & Henning 1994). For the temperatures we used the values of the rotational temperatures derived from the CH$_3$CN observations (see Section 5.1.2). For cores in which no rotational
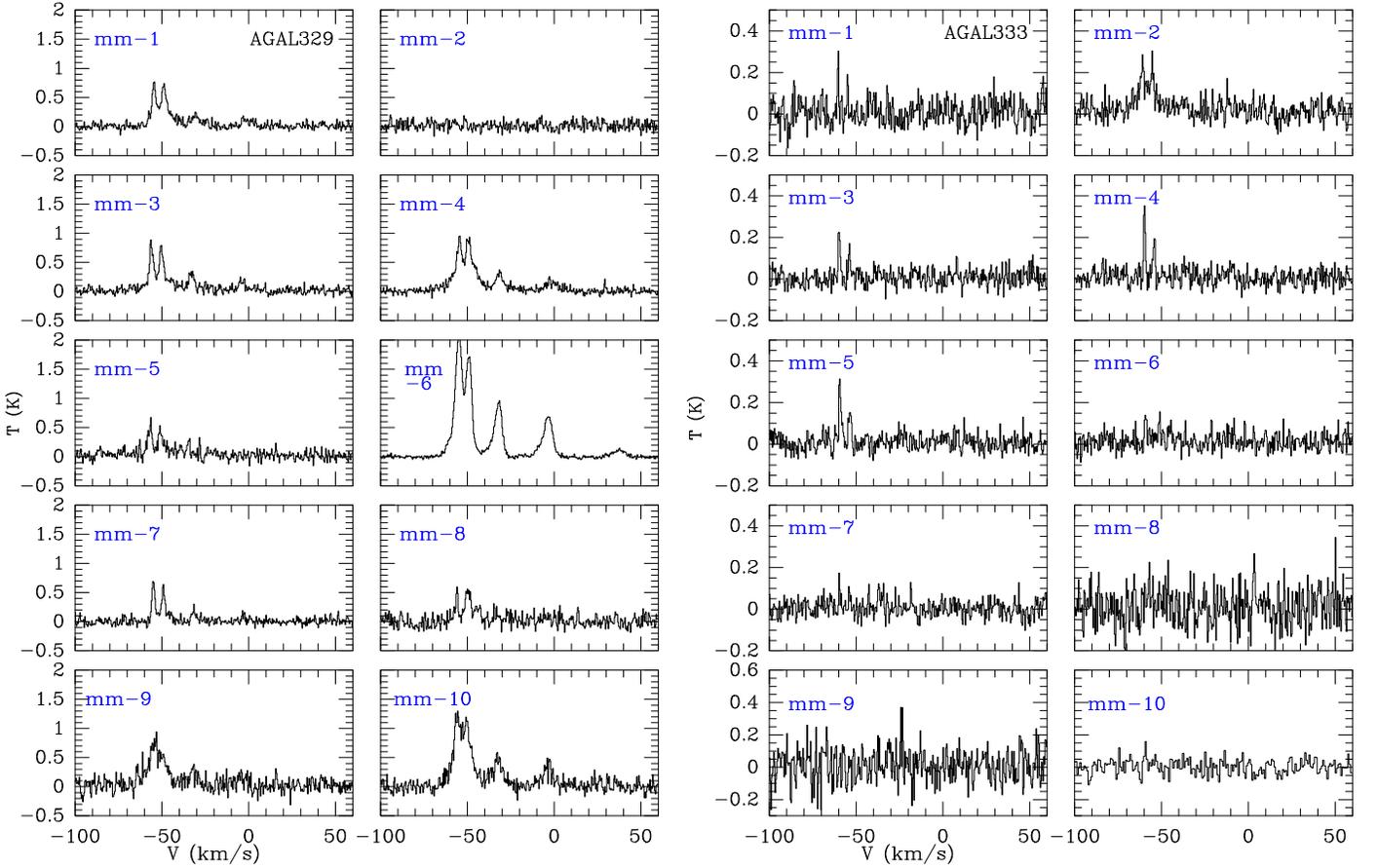
Figure 12. Average spectra of the CH_3CN emission from cores. Left: AGAL329 cores. Right: AGAL333 cores.

temperature is available we adopted the temperature of the clump. The masses, listed in Column 3 of Table 7, range from 1.6–20 $M_\odot$ for cores in the prestellar clump and from 1.7–119 $M_\odot$ for cores in the protostellar clump. The uncertainties in the mass are estimated to be $\sim$40%, considering errors in the flux density, temperature, distance, and dust mass absorption coefficient (see Sanhueza et al. 2017). It is worth noting that to compute the mass of the central core in AGAL329, we subtracted from the observed flux density at 100 GHz, the expected contribution from free–free emission. The latter was determined from an extrapolation of the observed flux densities at 18 and 22 GHz (Sánchez-Monge et al. 2013). The total mass in the form of cores is $\sim$6% of the clump mass in the prestellar clump and $\sim$23% in the protostellar clump.

5.1.4. Column Densities

The source averaged H_2 column densities of the cores can be computed from the continuum flux density, S_ν, using the expression,

$$N_{H_2} = \frac{S_\nu R_{gd}}{\Omega_c \mu_{H_2} m_H k_\nu B(T, \nu)}, \quad (6)$$

where $\mu_{H_2} = 2.8$ is the molecular weight per hydrogen molecule, m_H is the H-atom mass, and Ω_c is the solid angle subtended by the core. Column 4 of Table 10 lists the source averaged column densities, computed using the flux density measured in circular regions with the angular radius given in Column 3 and as dust temperature the CH_3CN rotational

temperature of the cores (or clump temperature for cores in which rotational temperature is not available). They range from 6.0×10^{22}–2.6×10^{23} cm^{-2} for cores in the prestellar clump and from 1.0×10^{23}–7.5×10^{23} cm^{-2} for cores in the protostellar clump. The highest values of the H_2 column densities are found toward the centrally located cores, mm-6 in AGAL329 and mm-5 in AGAL333. The uncertainties in the column densities are estimated to be $\sim$35%.

From the observations of the N_2H^+ line emission it is possible to compute the source averaged column densities using the expression (e.g., Garden et al. 1991; Mangum & Shirley 2015),

$$N_{tot}(N_2H^+)$$
$$= \frac{3k}{8\pi^3\mu^2 B} \frac{(T_{ex} + hB/3k)}{J_u} \frac{\exp(\frac{E_u}{kT_{ex}})}{\exp(h\nu/kT_{ex}) - 1} \int \tau_\nu dv, \quad (7)$$

where, E_u is the upper level energy, B is the rotational constant of the molecule, T_{ex} is the excitation temperature, ν is the frequency, μ is the dipole moment, Q_{rot} is the partition function, k is the Boltzmann constant, h is the Planck constant, and τ is the total optical depth. For observations of the $J = 1 \rightarrow 0$ line,

$$N_{tot}(N_2H^+) = 3.10 \times 10^{11}$$
$$\times (T_{ex} + 0.74) \frac{\exp(\frac{4.47}{T_{ex}})}{\exp(\frac{4.47}{T_{ex}}) - 1} \int \tau_\nu dv \text{ cm}^{-2}, \quad (8)$$
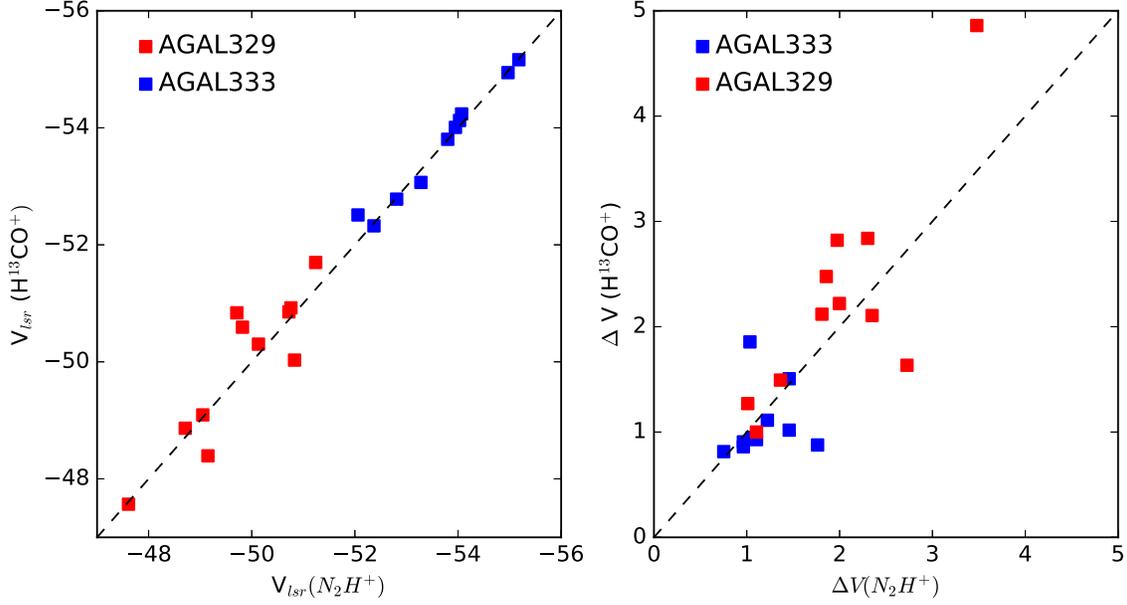
where dv is in km s^{-1}.

Figure 13. Comparison between the line velocities (left panel) and line widths (right panel) derived from the N_2H^+ HF fit and the $H^{13}CO^+$ Gaussian fit. Blue and red squares indicate values for cores in AGAL333 and in AGAL329, respectively.

Table 6
Line Parameters of the Core Emission in Optically Thin Lines

Core	N_2H^+ $J = 1 \rightarrow 0$			$H^{13}CO^+$ $J = 1 \rightarrow 0$		
	V_{lsr} (km s^{-1})	ΔV (km s^{-1})	τ_{tot}	V_{lsr} (km s^{-1})	ΔV (km s^{-1})	T_A (K)
			AGAL329			
mm-1	-48.71 ± 0.04	2.35 ± 0.09	10.0 ± 1.4	-48.87 ± 0.04	2.11 ± 0.09	2.55 ± 0.09
mm-2	-50.72 ± 0.02	1.01 ± 0.05	10.1 ± 1.3	-50.85 ± 0.11	1.27 ± 0.27	0.95 ± 0.17
mm-3[a]	-50.76 ± 0.09	1.09 ± 0.24	$\cdots$	-50.92 ± 0.03	1.00 ± 0.07	2.25 ± 0.13
mm-4[a]	-49.05 ± 0.10	2.29 ± 0.02	$\cdots$	-49.09 ± 0.02	2.84 ± 0.04	2.23 ± 0.10
mm-5	-51.24 ± 0.02	2.00 ± 0.05	5.2 ± 0.5	-51.70 ± 0.09	2.22 ± 0.22	1.27 ± 0.11
mm-6	-49.82 ± 0.20	3.48 ± 0.35	1.1 ± 0.4	-50.59 ± 0.05	4.86 ± 0.12	3.36 ± 0.04
	-47.61 ± 0.05	1.36 ± 0.21	0.5 ± 0.1	-47.57 ± 0.02	1.49 ± 0.07	2.53 ± 0.11
mm-7	-49.15 ± 0.02	1.81 ± 0.05	9.6 ± 0.9	-48.39 ± 0.13	2.12 ± 0.30	0.81 ± 0.10
mm-8	-50.13 ± 0.05	1.86 ± 0.14	2.7 ± 1.0	-50.30 ± 0.07	2.48 ± 0.17	2.56 ± 0.15
mm-9	-49.71 ± 0.03	2.72 ± 0.07	2.2 ± 0.4	-50.03 ± 0.16	2.82 ± 0.38	1.29 ± 0.15
mm-10	-50.83 ± 0.02	1.97 ± 0.07	3.6 ± 0.5	-50.84 ± 0.04	1.63 ± 0.09	3.97 ± 0.19
			AGAL333			
mm-1	-54.97 ± 0.01	0.75 ± 0.02	4.0 ± 0.5	-54.94 ± 0.06	0.81 ± 0.14	1.14 ± 0.17
mm-2	-55.18 ± 0.01	1.03 ± 0.05	4.0 ± 0.6	-55.16 ± 0.09	1.86 ± 0.21	1.23 ± 0.12
mm-3	-54.03 ± 0.02	1.46 ± 0.05	1.4 ± 0.4	-54.13 ± 0.05	1.51 ± 0.11	1.61 ± 0.10
mm-4	-54.07 ± 0.01	0.96 ± 0.02	12.5 ± 1.3	-54.24 ± 0.02	0.91 ± 0.06	2.13 ± 0.12
mm-5	-53.80 ± 0.01	1.22 ± 0.02	4.7 ± 0.5	-53.80 ± 0.05	1.11 ± 0.11	1.31 ± 0.11
mm-6	-52.81 ± 0.01	1.10 ± 0.02	3.4 ± 0.5	-52.78 ± 0.04	0.93 ± 0.09	1.70 ± 0.14
mm-7	-53.95 ± 0.03	1.46 ± 0.07	2.6 ± 0.8	-54.01 ± 0.03	1.02 ± 0.07	1.70 ± 0.10
mm-8	-52.37 ± 0.02	0.96 ± 0.05	8.0 ± 1.3	-52.32 ± 0.10	0.86 ± 0.24	0.91 ± 0.22
mm-9	-52.10 ± 0.01	1.50 ± 0.05	2.8 ± 0.4	$\cdots$	$\cdots$	$\cdots$
mm-10	-53.28 ± 0.01	1.06 ± 0.02	2.3 ± 0.4	-53.07 ± 0.04	0.95 ± 0.10	1.91 ± 0.17

Note.
[a] N_2H^+ line velocity and widths is obtained from the Gaussian fit to the lower velocity component.

Column 5 of Table 10 lists the N_2H^+ column densities of the cores computed from the above relation using the line widths and total optical depths determined from the HF fit. For the temperature, we adopted the CH_3CN rotational temperature of the cores. For cores for which no rotational temperature is available the temperature of the clump was used. As shown in Figure 17, which plots the H_2 versus N_2H^+ column densities, cores in the protostellar clump have typically larger H_2 and

Table 7
Derived Core Parameters

Core	Temp. (K)	Mass ($M_\odot$)	Radius (pc)	Radius (10^3 au)	$n(H_2)$ (10^7 cm^{-3})	σ_{vir} [a] (km s^{-1})	M_{vir} ($M_\odot$)	α_{vir}
					Derived Parameters			
				AGAL329				
mm-1	30	14.8	0.011	2.3	3.9	1.05	14.0	0.95
mm-2	28	1.7	0.005	1.0	4.6	0.53	1.6	0.96
mm-3	41	11.6	0.012	2.5	2.3	0.59	4.9	0.42
mm-4	34	27.2	0.019	3.9	1.4	1.03	23.4	0.86
mm-5	33	3.0	0.008	1.7	2.0	0.91	7.7	2.60
mm-6	68	118.8[b]	0.030	6.2	1.5	1.55	84.2	0.71
mm-7	31	3.1	0.009	1.9	1.5	0.83	7.3	2.38
mm-8	28	8.5	0.013	2.7	1.3	0.85	10.9	1.28
mm-9	28	9.3	0.021	4.3	0.4	1.20	34.9	3.74
mm-10	41	20.1	0.011	2.3	5.3	0.91	10.7	0.53
				AGAL333				
mm-1	22	1.6	0.006	1.2	2.6	0.42	1.2	0.74
mm-2	31	6.3	0.011	2.3	1.6	0.54	3.8	0.60
mm-3	22	2.4	0.010	2.1	0.8	0.68	5.3	2.25
mm-4	30	11.4	0.022	4.5	0.4	0.51	6.8	0.59
mm-5	24	19.8	0.016	3.3	1.7	0.59	6.5	0.33
mm-6	22	7.1	0.009	1.9	3.4	0.54	3.0	0.43
mm-7	22	3.0	0.014	2.9	0.4	0.68	7.5	2.50
mm-8	22	2.9	0.007	1.4	3.0	0.49	1.9	0.66
mm-9	22	2.2	0.006	1.2	3.5	0.80	4.4	2.04
mm-10	22	3.5	0.016	3.3	0.3	0.52	5.1	1.46

Notes.

[a] $\sigma_{vir} = \sqrt{(\sigma_{th}^2 + \sigma_{tur}^2)}$, where σ_{th} is the thermal width and σ_{tur} is the turbulent width.

[b] Computed from the observed flux density at 3 mm corrected by the contribution from the free–free emission.

N_2H^+ column densities than cores in the prestellar clump. The average N_2H^+ column density of the cores in the prestellar and prostellar clumps are, respectively, 2.3×10^{14} and 7.6×10^{14} cm^{-2} and the average H_2 column densities are 1.3×10^{23} and 3.5×10^{23} cm^{-2}. The average abundance of N_2H^+ relative to H_2, computed as the ratio of the respective column densities, are 1.9×10^{-9} and 3.1×10^{-9} for cores in the prestellar and protostellar clumps, respectively, indicating that in protostellar cores the abundance of N_2H^+ is typically larger than in prestellar cores. An increase in the N_2H^+ abundance with evolutionary stage has also been reported for clumps (e.g., Sanhueza et al. 2012; Hoq et al. 2013).

5.2. Mass Distribution

Figure 18 shows the distribution of the core masses in each clump. The dotted line indicates the value of the Jeans mass at the average clump conditions (see Table 1). The masses of the cores are of the order or slightly higher than the clump Jeans mass, except for the central core in AGAL329, which highly exceeds the Jeans mass. The number of cores detected in each clump ($\sim$10) is much smaller than the number of thermal Jeans masses contained in the clumps, of $\sim$160, showing that fragmentation is not efficient during the early stages of evolution. This conclusion has been previously reported by Csengeri et al. (2017), who found that the fragmentation of infrared quiet MDCs at scales of 0.06–0.3 pc is limited, with most clumps hosting typically three cores with masses of $\geqslant$40 $M_\odot$.

Our observations with a spatial resolution of $\sim$0.03 pc, 10 times smaller than that of Csengeri et al. (2017), show that the number of cores per clump increases to 10, suggesting that we are resolving further fragmentation within MDCs. Recent studies of clumps with similar characteristics to those observed by Csengeri et al. (2017) have reported levels of fragmentation ranging from five to 20 cores when observed at scales of 0.03–0.05 pc (e.g., Contreras et al. 2018; Lu et al. 2018).

Figure 19 shows the normalized cumulative distribution function (CDF), also known as empirical cumulative distribution function (eCDF). We prefer to use the eCDF over the differential form of the core mass function (CMF) because the latter approach contains the numerical bias introduced by binning. Given the relatively small number of cores detected in each clump, we considered the combined sample of cores in the prestellar and protostellar clumps including, in addition, the cores detected by Servajean et al. (2019) toward the prestellar clump (AGAL305), which have similar characteristics to the clumps considered here. We adopt here as mass sensitivity limit the mass computed using a flux density equal to the 3σ noise level and the temperature of the clump. The mass sensitivity limits are 0.9, 0.7, and 1.4 $M_\odot$ for AGAL329, AGAL333, and AGAL305, respectively.

Assuming that the CMF can be described by a power law $dN/dM \propto M^\alpha$, the value of the α index that best reproduces the eCDF, using the maximum likelihood method (see Servajean et al. 2019), is -1.33 ± 0.15, and the 90% confidence interval is -1.58 to -1.08. This power-law index is much shallower than that of the initial stellar mass function
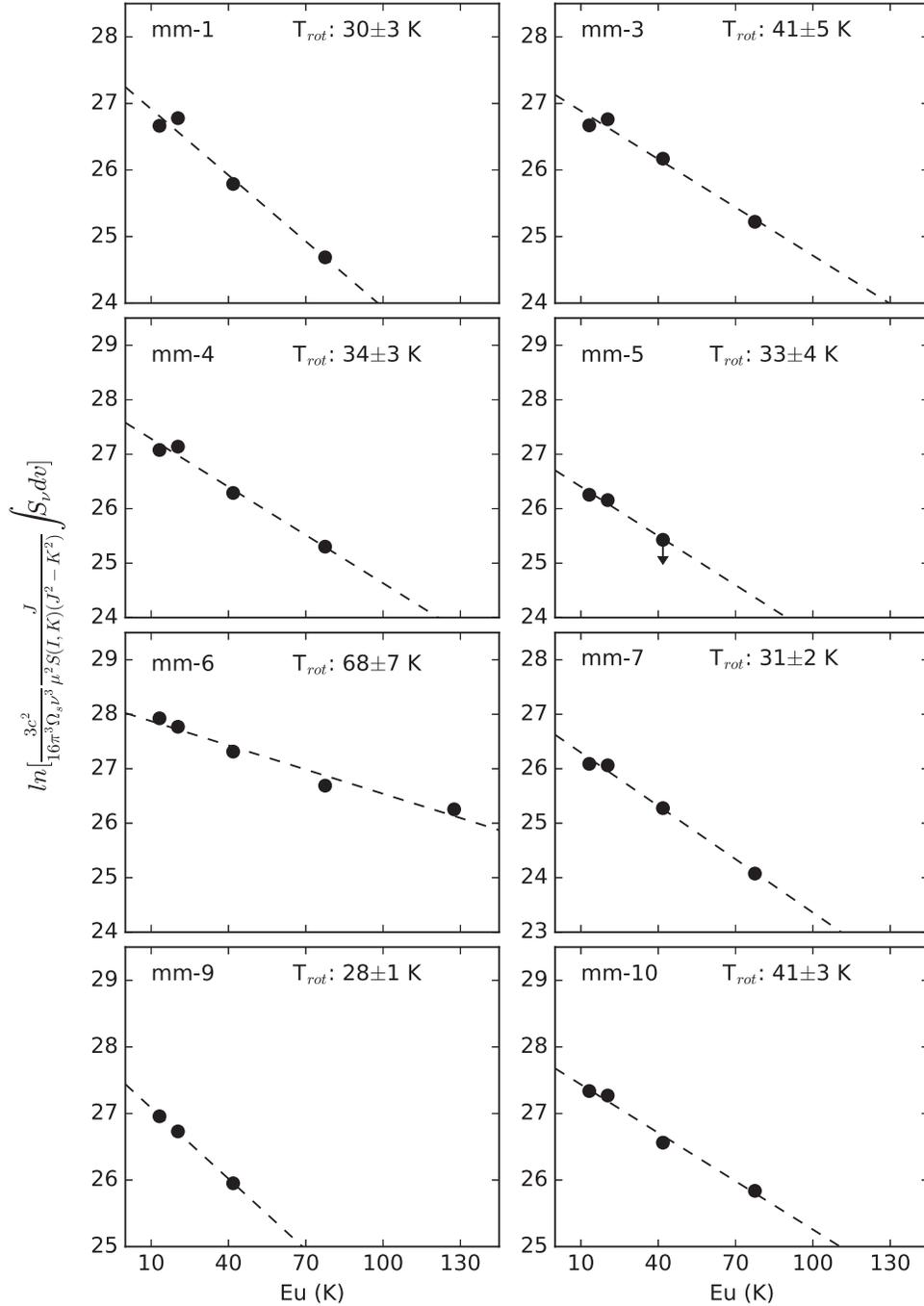
Figure 14. CH_3CN rotational diagram for cores in the protostellar clump. The derived rotational temperature is given in the upper right corner.

(IMF) for stars with masses greater than 1 $M_\odot$, of -2.35 (Kroupa 2001), suggesting that in the early stage of fragmentation of clumps, high-mass cores are more efficiently formed than low mass cores. Our result is alike to that of the recently reported ALMA study of CMF toward the high-mass star-forming region W43-MM1 (Motte et al. 2018b) and toward infrared dark clouds (Liu et al. 2018) indicating the top-heavy nature of CMF in high-mass star-forming regions.

5.3. Dynamical State

To assess the dynamical state of the cores we compute the virial parameter, α_{vir}, defined as $\alpha_{vir} = M_{vir}/M_{dust}$, where M_{vir}

is the virial mass defined as

$$M_{vir} = \frac{5\sigma^2 R}{G},\qquad(9)$$

where $\sigma = \sqrt{(\sigma_{th}^2 + \sigma_{tur}^2)}$, σ_{th} and σ_{tur} are the thermal and turbulent velocity dispersions, respectively, R is the radius, and G the gravitational constant. The turbulent velocity dispersion was computed from the observed N_2H^+ or $H^{13}CO^+$ line widths and the thermal velocity dispersion was computed using the temperature given in Column 2 of Table 7 for a particle with a molecular weight of 2.33 (e.g., Bertoldi & McKee 1992). The virial mass and virial parameter of the cores are given in
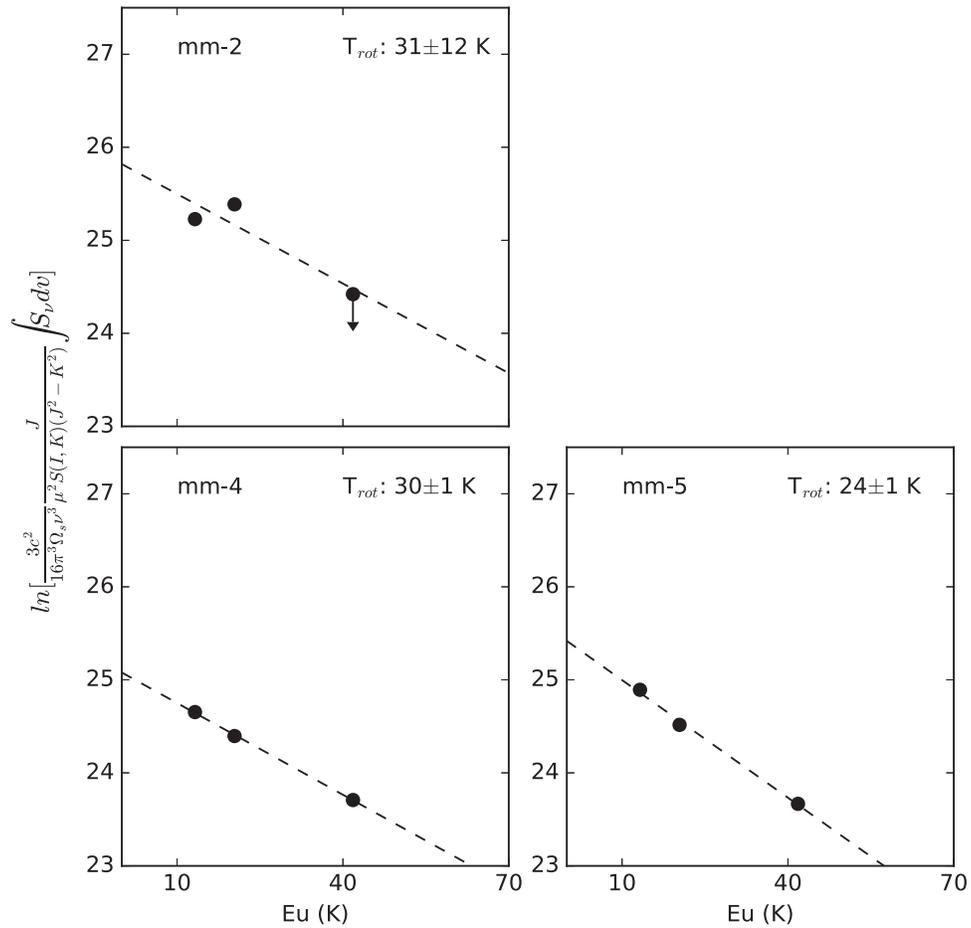
Figure 15. CH$_3$CN rotational diagram for cores in the prestellar clump. The derived rotational temperature is given in the upper right corner.

Table 8
Observed and Derived Parameters from CH$_3$CN Observations

Core	Velocity Integrated Flux Density (Jy km s^{-1})					θ ($''$)	T_{rot} (K)	N_t(CH$_3$CN) (10^{14} cm^{-2})
	$K = 0$	$K = 1$	$K = 2$	$K = 3$	$K = 4$			
AGAL329								
mm-1	0.22	0.24	0.08	0.04	⋯	2.0	30 ± 3	4.4 ± 1.0
mm-2	⋯	⋯	⋯	⋯	⋯	⋯	⋯	⋯
mm-3	0.22	0.23	0.11	0.07	⋯	2.0	41 ± 5	6.3 ± 1.3
mm-4	0.33	0.34	0.13	0.07	⋯	2.0	34 ± 3	7.3 ± 1.4
mm-5	0.15	0.13	0.05	⋯	⋯	2.0	33 ± 4	3.0 ± 0.7
mm-6	5.90	4.89	2.62	2.09	0.34	5.0	68 ± 7	32.1 ± 6.5
mm-7	0.12	0.12	0.05	0.02	⋯	2.0	31 ± 2	2.4 ± 0.3
mm-8	⋯	⋯	⋯	⋯	⋯	⋯	⋯	⋯
mm-9	0.17	0.13	0.05	⋯	⋯	2.0	28 ± 1	4.8 ± 0.2
mm-10	0.43	0.39	0.17	0.12	⋯	2.0	41 ± 3	11.0 ± 1.7
AGAL333								
mm-2	0.08	0.09	0.03	⋯	⋯	2.5	31 ± 12	1.1 ± 0.7
mm-4	0.07	0.05	0.02	⋯	⋯	2.0	30 ± 1	0.51 ± 0.03
mm-5	0.04	0.02	0.01	⋯	⋯	3.0	24 ± 1	0.50 ± 0.06

Columns 8 and 9 of Table 7, respectively. Given the uncertainties in the values of the quantities that enter into the calculation of α_{vir} we consider that cores that have $0.71 < \alpha_{vir} < 1.4$ are in virial equilibrium (i.e., we are considering an error of up to 40%).

In the prestellar clump, five cores are sub-virial (i.e., $\alpha_{vir} \leqslant 0.7$), indicating that their gravitational energy dominates their kinetic energy, and in the absence of other means of support (e.g., magnetic energy), they are likely to be undergoing gravitational collapse. Two cores are in virial equilibrium and the three others have $\alpha_{vir} \geqslant 1.5$, suggesting that they may correspond to transient features. In the protostellar clump, five cores are in virial equilibrium, two are sub-virial, and three have $\alpha_{vir} \geqslant 1.5$.
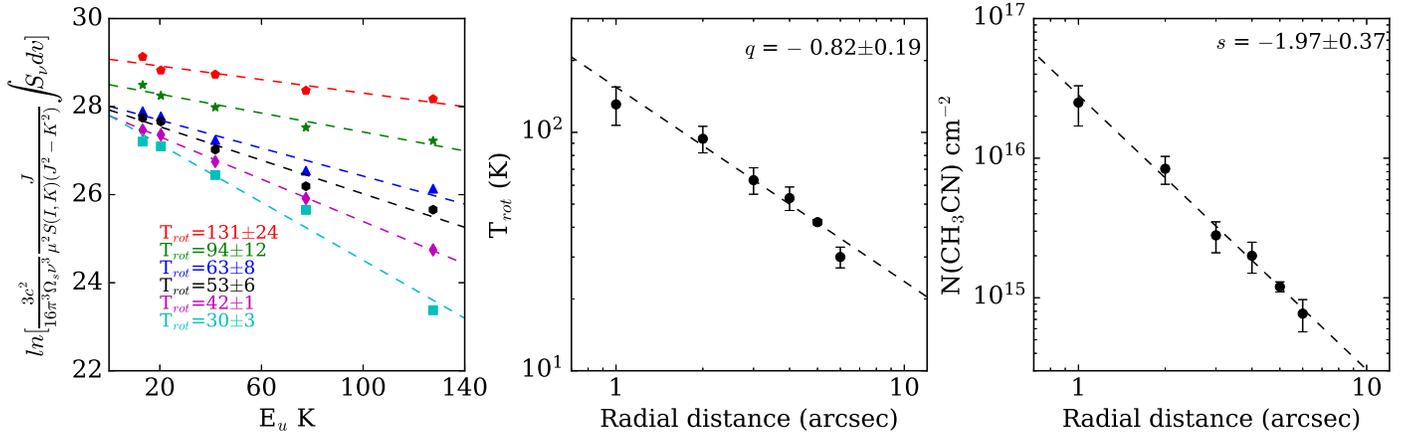
Figure 16. Left: rotational diagram of the CH$_3$CN emission from six different regions within core mm-6 in AGAL329 (see the text for the description of the regions). The derived rotational temperatures are shown in the lower left corner. Middle: rotational temperature dependence with radius. Right: CH$_3$CN column density dependence with radius.

Table 9
Observed and Derived Parameters from CH$_3$CN Observations toward Core mm-6 in AGAL329

Region	Velocity Integrated Flux Density (Jy km s^{-1})					Ω_{eff} [a] ($''^2$)	T_{rot} (K)	N_t(CH$_3$CN) (10^{15} cm^{-2})
	$K=0$	$K=1$	$K=2$	$K=3$	$K=4$			
1	0.65	0.46	0.36	0.39	0.09	3.1	131 ± 24	25.4 ± 8.1
2	1.03	0.77	0.52	0.50	0.10	9.1	94 ± 12	8.4 ± 1.9
3	0.94	0.81	0.41	0.31	0.06	15.2	63 ± 8	2.8 ± 0.7
4	1.14	1.00	0.46	0.31	0.05	21.2	53 ± 6	2.0 ± 0.5
5	1.10	0.95	0.45	0.30	0.03	28.3	42 ± 1	1.2 ± 0.1
6	1.04	0.90	0.41	0.28	0.01	31.2	30 ± 3	0.8 ± 0.2

Note.
[a] Effective solid angle of the region.

5.4. The Massive Core at the Center of the Protostellar Clump

The massive (119 $M_\odot$) core located at the center of the protostellar clump has a virial parameter of 0.71, suggesting it is gravitationally bound and could be undergoing gravitational collapse. This hypothesis is strongly supported by the observed profiles in the optically thick HCO$^+$ line, which exhibits a double-peaked profile with the blueshifted peak being brighter than the redshifted peak, and in the optically thin H^{13}CO$^+$ line, which shows a single peak profile with a peak velocity near the dip in HCO$^+$ (see Figure 20). These characteristics of the line profiles are a classical signature of infalling motions (see Mardones et al. 1997).

To estimate the infall velocity we fitted the observed HCO$^+$ core spectrum with analytical infall models presented by De Vries & Myers (2005). The best fit is attained with the "Hill5" model (see Figure 20), which assumes that the excitation temperature increases inwards as a linear function of the optical depth, indicating an infall velocity, v_{in}, of 1.6 km s^{-1}. We note that none of the simple models is able to reproduce the observed deep absorption feature (reaching zero intensity). To reproduce it requires a more sophisticated modeling, which is beyond the scope of this work. From the derived values of the infall speed (1.6 km s^{-1}), core radius (0.03 pc), molecular weight μ_{H_2} (2.8), and molecular hydrogen density (1.5×10^7 cm^{-3}) we estimate a mass infall rate $\dot{M}$ (= 4 $\pi R^2 n(H_2) \mu_{H_2} m_H v_{in}$) of 1.9×10^{-2} $M_\odot$ yr^{-1}, a value similar to those reported in other high-mass star-forming regions (e.g., Beuther et al. 2002; Garay et al. 2002; Contreras et al. 2018).

The observed radial intensity profile of the massive core, shown in Figure 21, deviates significantly from a Gaussian profile but is well approximated with a Plummer-like radial intensity profile of the form,

$$I(I_0, R_0, p) = \frac{I_0}{\left(1 + \left(\frac{R}{R_0}\right)^2\right)^{\frac{p}{2}}}, \tag{10}$$

where p is the power-law index, I_0 is the peak intensity, and R_0 is the Plummer radius. The best fit (shown as a red line) indicates a power-law index p of 2.2 ± 0.1 and R_0 of 0.95 ± 0.05$''$. Whitworth & Ward-Thompson (2001) have already shown that the density profile of cores undergoing collapse can be successfully fit with Plummer-like profiles.

In summary, the observed and derived properties of this massive core, e.g., collapse and outflow signatures, high-mass infall rate, and Plummer-like density profile, are consistent with a picture in which large-scale collapse is feeding gas into this core, which is forming a massive protostar at its center.

5.5. Comparison with Models of the Fragmentation of Clumps and the Formation of High-mass Stars

The formation of a cluster of stars is thought to proceed through a sequence of fragmentation, merging, and a collapse process within MDCs (e.g., Vázquez-Semadeni et al. 2009; Motte et al. 2018a). Given the complexity of this process most of the recent advances in this field have been made through numerical simulations. To better constrain the models, and

Table 10
Source Averaged H_2 and N_2H^+ Column Densities

Core	S_ν (mJy)	θ ($''$)	$N(H_2)$ (10^{23} cm^{-2})	$N(N_2H^+)$ (10^{14} cm^{-2})	$X(N_2H^+)$ (10^{-9})
			AGAL329		
mm-1	5.1	2.5	3.9	16.1	4.2
mm-2	0.9	2.0	1.1	6.2	5.4
mm-3	5.8	3.0	2.2	⋯	⋯
mm-4	10.7	3.0	4.9	⋯	⋯
mm-5	2.1	3.0	1.0	8.6	8.5
mm-6	93.8	5.0	7.5	12.4	1.7
mm-7	1.5	2.0	1.8	2.1	1.2
mm-8	3.3	3.0	1.9	3.0	1.6
mm-9	1.7	1.5	3.9	3.6	0.9
mm-10	8.4	2.0	7.1	8.9	1.3
Average			3.5	7.6	3.1
			AGAL333		
mm-1	0.7	2.5	0.7	1.1	1.6
mm-2	2.4	3.0	1.2	3.0	2.5
mm-3	1.4	3.0	1.0	0.8	0.8
mm-4	2.8	3.0	1.5	8.3	5.5
mm-5	3.8	3.0	2.6	2.6	1.0
mm-6	1.7	2.5	1.8	1.4	0.8
mm-7	1.3	3.5	0.7	1.4	2.1
mm-8	0.9	2.0	1.4	3.0	2.1
mm-9	0.7	2.0	1.1	0.8	0.7
mm-10	1.1	3.5	0.6	0.9	1.6
Average			1.3	2.3	1.9

Table 11
Summary of Core Characteristics

	Prestellar Clump AGAL333	Protostellar Clump AGAL329
Number of cores	10	10
Mean core size	0.012 pc	0.014 pc
Mean velocity dispersion	0.50 km s^{-1}	0.85 km s^{-1}
ΣM_{cores}	60 $M_\odot$	218 $M_\odot$
$f(\Sigma M_{\text{cores}}/M_{\text{clump}})$	0.06	0.23
$M_{\text{centralcore}}$	20 $M_\odot$	119 $M_\odot$
$f(M_{\text{centralcore}}/\Sigma M_{\text{cores}})$	0.33	0.55
$f(M_{\text{centralcore}}/M_{\text{clump}})$	0.02	0.13

Figure 17. H_2 column densities vs. N_2H^+ column densities for prestellar cores (blue squares) and protostellar cores (red squares). Typical errors in column densities are shown in the lower right corner.

Figure 18. Core mass distribution. Upper panel: AGAL333. Bottom panel: AGAL329. The dotted line indicates the Jeans mass at the average conditions of the clump.

hence to understand the formation of stars, it is crucial to know the initial conditions of the sequence. In particular, the properties of the cores at the early stages of evolution of MDCs are poorly known.

Our ALMA observations of the two MDC in early stages of evolution, with spatial resolutions of ∼0.02 pc, allowed us to determine the characteristics of the fragmentation at early stages of evolution, such as the number of cores, their physical and kinematical characteristics, and the initial CMF. Both clumps have masses of ∼10^3 $M_\odot$ and therefore can potentially form a cluster of stars, and in particular, from the empirical mass-size relationship (Kauffmann et al. 2010) will probably give rise to high-mass stars. Thus, we can compare our findings with models of massive star and cluster formation, although we note that few of them have made predictions concerning the fragmentation at early stages of clump evolution. We recall that
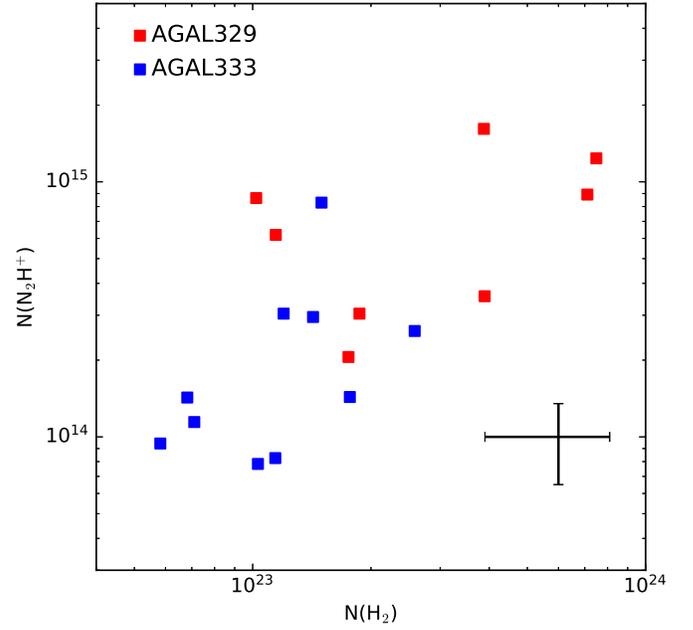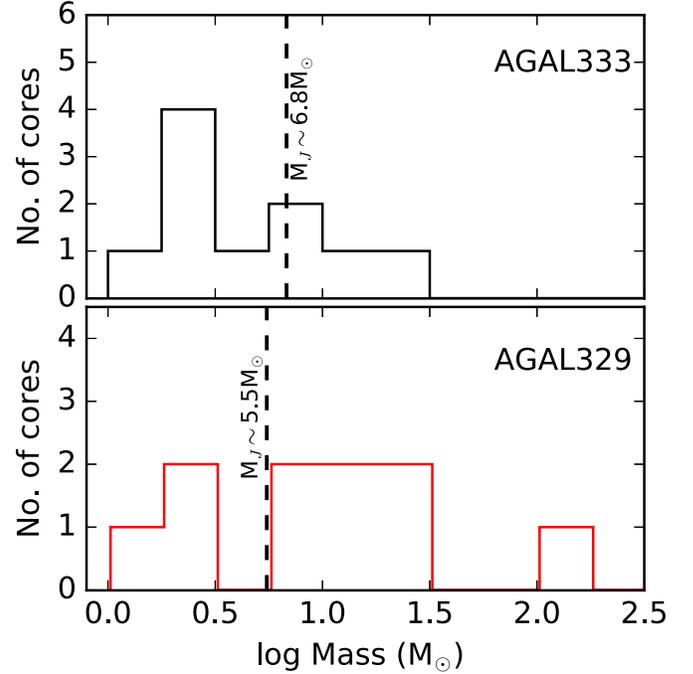
one clump is in the prestellar stage and the other in the protostellar stage, thus, we can investigate differences in the cores due to evolution.

The competitive accretion model (Bonnell 2002; Bonnell & Bate 2006) proposes that a clump initially fragments into cores of thermal Jeans masses. These cores then accrete mass from the reservoir material in the clump via Bondi–Hoyle accretion. Cores located near the center of the gravitational potential accrete at a higher rate leading to the formation of a high-mass
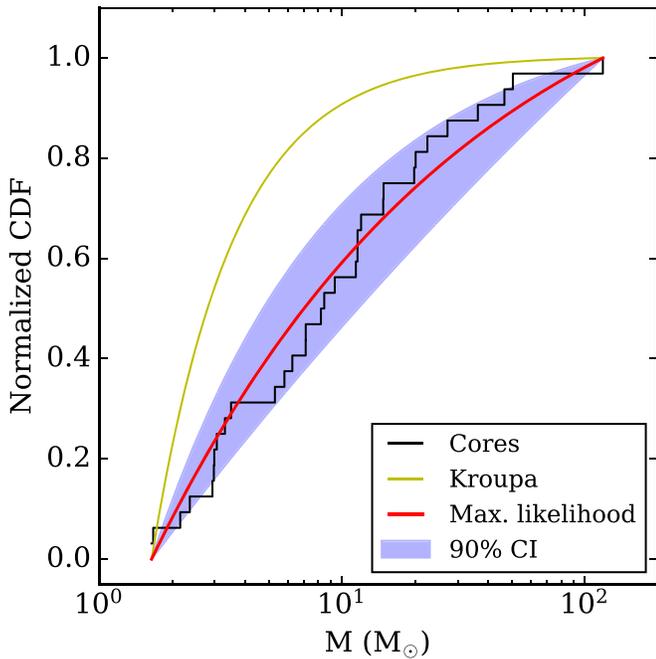
Figure 19. The normalized CDF for the combined sample of cores within clumps AGAL333, AGAL329, and AGAL305. The red line and purple-shaded area show the maximum likelihood estimation of the power-law index fit and its 90% confidence interval, respectively. The yellow line shows the initial mass function distribution from Kroupa (2001).
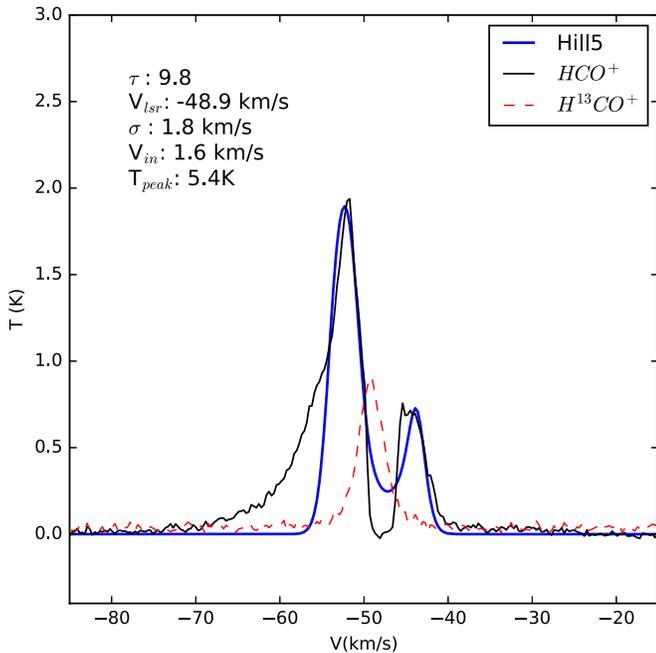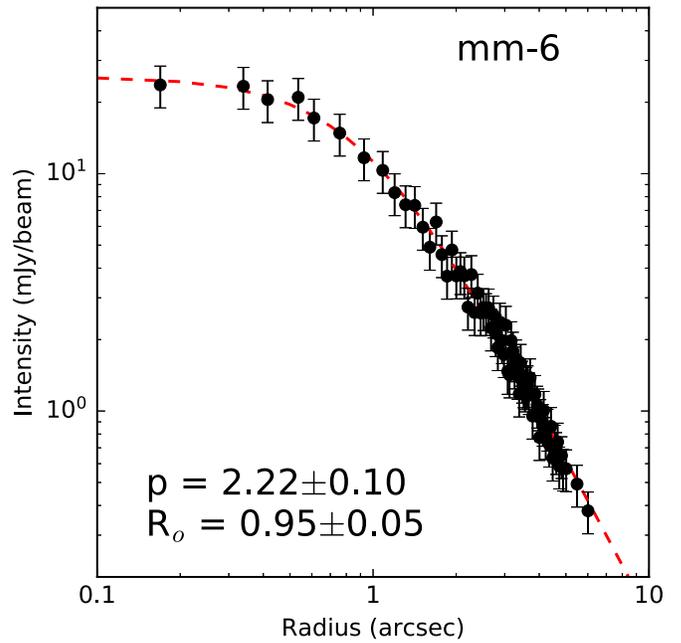

Figure 21. Radial intensity profile of the massive core (mm-6) at the center of AGAL329. The dotted red line correspond to a fit with a Plummer-like profile. Error bars correspond to 10% errors in the observed intensities.

Figure 20. Average spectra of the HCO^+ (black line) and $H^{13}CO^+$ (red line) emissions from the central massive core in AGAL329. The blue line shows the best fit using the analytical infall models of De Vries & Myers (2005). Fitted parameters are given in the upper left corner.

turbulence and/or magnetic fields and hence should have masses much larger than the thermal Jeans mass. In this model the core mass distribution is then set at early evolutionary times, and therefore shall be similar to the initial stellar mass distribution (Tan et al. 2014). In addition, in this scenario cores are expected to be virialized (McKee & Tan 2002; Krumholz & Bonnell 2009).

We found that the number of cores detected in both clumps is considerably smaller than the number of thermal Jeans masses contained in the clumps ($M/M_J \sim 160$), showing that fragmentation is not efficient during the early stages of evolution. In addition, the fraction of total core mass to clump mass is 6% in the prestellar clump and rises to $\sim 23\%$ in the protostellar clump. Because the number of cores in both clumps is similar, and the fact that the masses of the cores in the protostellar clump are typically higher than the masses of the cores in the prestellar clump, which are of the order of the clump Jeans mass, supports the hypothesis of a continuous increase in core masses due to accretion from the prestellar to the protostellar stage.

A large fraction of the cores within the prestellar clump (five out of 10) are sub-virial ($\alpha < 0.7$), two are virialized ($0.7 < \alpha < 1.4$) and the remaining three (with $\alpha \geqslant 1.5$) are most likely transient features. On the other hand, five out of 10 cores in the protostellar clump are virialized and two are in sub-virial states.

These results support the view of a globally collapsing turbulent clump undergoing gravitational fragmentation. In this scenario, during the early stages of evolution (AGAL333 clump) most of the formed cores should have masses typical of the thermal Jeans mass and be in sub-virial states. In a more advanced stage (AGAL329 clump), the gas is funneled down to the center of the potential and the centrally located core continues to accrete gas at a high rate, becoming the most massive one.

protostar. In the competitive accretion scenario cores in an early stage after the fragmentation are expected to be sub-virial.

The turbulent core accretion model (McKee & Tan 2003) proposes that stars form via a monolithic collapse of cores in virial equilibrium supported by the internal pressure due to

6. Summary

We carried out ALMA Band 3 observations of 3 mm dust continuum and molecular emission, in lines of HCO$^+$, H^{13}CO$^+$, N$_2$H$^+$, and CH$_3$CN, toward two MDCs in early, but distinct, stages of evolution, one in a prestellar stage (AGAL333.014-0.521) and the other in a protostellar stage (AGAL329.184-0.314). The goal was to reveal the physical and dynamical characteristics of the small-scale structures (or cores) within these clumps. Table 11 summarizes the characteristics of the cores. The results are summarized as follows.

(1) From the 3 mm continuum images we identified, using the *Clumpfind* and *Dendogram* algorithms, about 10 cores within each clump. The cores in the prestellar clump, which are mainly distributed in a long filamentary structure running from NE to SW across the clump, have dust derived masses from 1.6–20 $M_\odot$, sizes from 0.006–0.022 pc (1200–4500 au) and densities from 3.0×10^6–3.5×10^7 cm^{-3}. The cores in the protostellar clump have dust derived masses from 1.7–119 $M_\odot$, sizes from 0.005–0.030 pc (1000–6200 au) and densities from 4.0×10^6–5.3×10^7 cm^{-3}. The fraction of total core mass relative to the clump mass is ~6% in the prestellar clump and ~23% in the protostellar clump. Most cores in the prestellar clump have masses within a factor of a few from the Jeans mass of the clump. However, the total number of cores is significantly smaller than the number of Jeans masses in the clump, indicating that fragmentation is inefficient during the early stages of evolution of clumps.

(2) Molecular emission was detected toward both clumps in all four observed species. Of these, the N$_2$H$^+$ emission is the brightest and most extended one and the one that best correlates with the continuum emission morphology.

Prestellar clump. The morphologies of the N$_2$H$^+$ and H^{13}CO$^+$ emission from AGAL333 are similar, delineating a complex network of filamentary structures across the whole region. The velocity field of the N$_2$H$^+$ emission shows a significant velocity gradient, of 4.7 km s^{-1} pc^{-1}, in a NE–SW direction, across the whole clump. The mass required to explain this as due to gravitationally bound rotation is 460 $M_\odot$ within a radius of 0.45 pc. CH$_3$CN emission is only detected toward the NE region of this clump.

Protostellar clump. The morphologies of the line emission from AGAL329 are noticeably different in the four observed transitions. The N$_2$H$^+$ emission arises from a bright central region, with three distinct condensations, and an extended envelope of emission, which is highly correlated with the absorption feature seen in the 8 μm *Spitzer* image. The HCO$^+$ emission toward the central region, shows a banana-like morphology, which is roughly coincident with the two westernmost N$_2$H$^+$ condensations, but no HCO$^+$ emission is seen from the eastern N$_2$H$^+$ condensation. In addition, the HCO$^+$ image shows two conspicuous features: a bright clumpy structure, located ~18″ south of the central region, elongated in the NE–SW direction, (the south feature), and a weak V-shaped feature located ~10″ west from the central region (the west feature). The most prominent features in CH$_3$CN are a bright central region whose peak position coincides with the peak position of the central core mm-6, and a bright V-shaped region coincident with the west feature seen in HCO$^+$.

(3) Emission in the N$_2$H$^+$, HCO$^+$, and H^{13}CO$^+$ lines was detected toward all continuum cores within AGAL329 and all cores, except mm-9, in AGAL333. The line widths, determined from observations of the optically thin H^{13}CO$^+$ and N$_2$H$^+$ lines,

are usually smaller for cores within the prestellar clump than for cores within the protostellar clump. The average line widths are 1.2 and 2.0 km s^{-1} for the AGAL333 and AGAL329 cores, respectively. The explanation for the large line widths in cores within the protostellar clump is not straightforward, as it may reflect an increase in the level of turbulence due to the beginning of star formation activity, magnetic fields, or an increase in the gas velocities due to collapse motions. Emission in CH$_3$CN was detected from all continuum cores in the protostellar clump and only weak emission was detected toward five cores in the prestellar clump. The temperatures, derived from a rotational diagram analysis of the emission in the CH$_3$CN $J = 5_K$–4_K lines, range from 28–68 K for cores in the protostellar clump and from 24–31 K for cores in the prestellar clump.

(4) Five cores within AGAL333 exhibit inverse P Cygni profiles in the HCO$^+$ line and five are sub-virial (virial parameters smaller than 0.7), indicating that most cores within the prestellar clump seem to be undergoing contracting motions. Within AGAL329, most cores exhibit double-peak profiles in HCO$^+$, with a stronger blueshifted peak, and single peaked profiles in H^{13}CO$^+$, with a velocity in between those of the HCO$^+$ peaks. These pair of profiles in optically thick (HCO$^+$) and optically thin (H^{13}CO$^+$) lines are a signature of infalling gas, which we suggest is associated with the global collapse of the protostellar clump.

(5) The core at the center of the protostellar clump is the most massive one, has a Plummer-like intensity profile, and exhibits line profiles that are characteristic of infalling gas, indicating an infall velocity of 1.6 km s^{-1} and a mass infall rate of 1.9×10^{-2} $M_\odot$ yr^{-1}. These results convey the idea that this core is still acquiring mass via the gravitational focusing of gas from a globally collapsing clump toward its large potential well. In addition, this core is associated with a bipolar outflow in HCO$^+$ possibly driven by a recently formed high-mass protostar at its center.

(6) The CMF for the combined sample of cores within three clumps (AGAL329, AGAL333, and AGAL305 from Servajean et al. 2019) has a power-law index of -1.33 ± 0.15, much flatter than that of the IMF for stars with masses greater than 1 $M_\odot$. The top-heavy nature of the CMF suggests that at an early stage of clump fragmentation, high-mass cores are more efficiently formed than low mass cores.

In summary, we conclude that we are witnessing the evolution of dense gas in globally collapsing MDCs, with AGAL333 showing the initial stage of fragmentation, producing cores that are individually collapsing, while in AGAL329 we are seeing a later stage in which a considerable fraction of the gas has been gravitationally focused into the central region.

ORCID iDs

Sudeep Neupane ⓘ https://orcid.org/0000-0001-9596-9938
Yanett Contreras ⓘ https://orcid.org/0000-0002-6388-3635
Andrés E. Guzmán ⓘ https://orcid.org/0000-0003-0990-8990
Luis Felipe Rodríguez ⓘ https://orcid.org/0000-0003-2737-5681

References

André, P., Men'shchikov, A., Bontemps, S., et al. 2010, A&A, 518, L102
Anglada, G., Rodríguez, L. F., Cantó, J., Estalella, R., & López, R. 1987, A&A, 186, 280
Araya, E., Hofner, P., Kurtz, S., Bronfman, L., & DeDeo, S. 2005, ApJS, 157, 279
Armstrong, J. T., Ho, P. T. P., & Barrett, A. H. 1985, ApJ, 288, 159
Astropy Collaboration, Robitaille, T. P., Tollerud, E. J., et al. 2013, A&A, 558, A33
Beltrán, M. T., Brand, J., Cesaroni, R., et al. 2006, A&A, 447, 221
Bergin, E. A., & Langer, W. D. 1997, ApJ, 486, 316
Bertoldi, F., & McKee, C. F. 1992, ApJ, 395, 140
Beuther, H., Schilke, P., Menten, K. M., et al. 2002, ApJ, 566, 945
Blake, G. A., Sutton, E. C., Masson, C. R., & Phillips, T. G. 1987, ApJ, 315, 621
Bonnell, I. A. 2002, in ASP Conf. Ser. 267, Hot Star Workshop III: The Earliest Phases of Massive Star Birth, ed. P. Crowther (San Francisco, CA: ASP), 193
Bonnell, I. A., & Bate, M. R. 2006, MNRAS, 370, 488
Caselli, P., Myers, P. C., & Thaddeus, P. 1995, ApJL, 455, L77
Caselli, P., Walmsley, C. M., Zucconi, A., et al. 2002, ApJ, 565, 344
Contreras, Y., Garay, G., Rathborne, J. M., & Sanhueza, P. 2016, MNRAS, 456, 2041
Contreras, Y., Rathborne, J. M., Guzmán, A., et al. 2017, MNRAS, 466, 340
Contreras, Y., Sanhueza, P., Jackson, J. M., et al. 2018, ApJ, 861, 14
Contreras, Y., Schuller, F., Urquhart, J. S., et al. 2013, A&A, 549, A45
Cornwell, T. J. 2008, ISTSP, 2, 793
Csengeri, T., Bontemps, S., Wyrowski, F., et al. 2017, A&A, 600, L10
De Vries, C. H., & Myers, P. C. 2005, ApJ, 620, 800
Faúndez, S., Bronfman, L., Garay, G., et al. 2004, A&A, 426, 97
Fazio, G. G., Hora, J. L., Allen, L. E., et al. 2004, ApJS, 154, 10
Foster, J. B., Jackson, J. M., Barnes, P. J., et al. 2011, ApJS, 197, 25
Garay, G., Brooks, K. J., Mardones, D., Norris, R. P., & Burton, M. G. 2002, ApJ, 579, 678
Garden, R. P., Hayashi, M., Gatley, I., Hasegawa, T., & Kaifu, N. 1991, ApJ, 374, 540
Gildas Team 2013, GILDAS: Grenoble Image and Line Data Analysis Software, Astrophysics Source Code Library, ascl:1305.010
Ginsburg, A., & Mirocha, J. 2011, PySpeckit: Python Spectroscopic Toolkit, Astrophysics Source Code Library, ascl:1109.001
Goldsmith, P. F., & Langer, W. D. 1999, ApJ, 517, 209
Güsten, R., Walmsley, C. M., Ungerechts, H., & Churchwell, E. 1985, A&A, 142, 381
Guzmán, A. E., Sanhueza, P., Contreras, Y., et al. 2015, ApJ, 815, 130
Hernández-Hernández, V., Zapata, L., Kurtz, S., & Garay, G. 2014, ApJ, 786, 38
Hoq, S., Jackson, J. M., Foster, J. B., et al. 2013, ApJ, 777, 157
Hunter, J. D. 2007, CSE, 9, 90
Jackson, J. M., Rathborne, J. M., Foster, J. B., et al. 2013, PASA, 30, 57
Jones, P. A., Burton, M. G., Cunningham, M. R., et al. 2008, MNRAS, 386, 117
Kauffmann, J., Pillai, T., Shetty, R., Myers, P. C., & Goodman, A. A. 2010, ApJ, 716, 433

König, C., Urquhart, J. S., Csengeri, T., et al. 2017, A&A, 599, A139
Kroupa, P. 2001, MNRAS, 322, 231
Krumholz, M. R., & Bonnell, I. A. 2009, in Models for the Formation of Massive Stars, ed. G. Chabrier (Cambridge: Cambridge Univ. Press), 288
Liu, M., Tan, J. C., Cheng, Y., & Kong, S. 2018, ApJ, 862, 105
Lu, X., Zhang, Q., Liu, H. B., et al. 2018, ApJ, 855, 9
Mangum, J. G., & Shirley, Y. L. 2015, PASP, 127, 266
Mardones, D., Myers, P. C., Tafalla, M., et al. 1997, ApJ, 489, 719
Martin-Pintado, J., Bachiller, R., & Fuente, A. 1992, A&A, 254, 315
McKee, C. F., & Tan, J. C. 2002, Natur, 416, 59
McKee, C. F., & Tan, J. C. 2003, ApJ, 585, 850
McMullin, J. P., Waters, B., Schiebel, D., Young, W., & Golap, K. 2007, in ASP Conf. Ser. 376, Astronomical Data Analysis Software and Systems XVI, ed. R. A. Shaw, F. Hill, & D. J. Bell (San Francisco, CA: ASP), 127
Molinari, S., Swinyard, B., Bally, J., et al. 2010, PASP, 122, 314
Motte, F., Bontemps, S., & Louvet, F. 2018a, ARA&A, 56, 41
Motte, F., Nony, T., Louvet, F., et al. 2018b, NatAs, 2, 478
Myers, P. C. 2009, ApJ, 700, 1609
Ossenkopf, V., & Henning, T. 1994, A&A, 291, 943
Padoan, P., & Nordlund, Å. 2002, ApJ, 576, 870
Palau, A., Ballesteros-Paredes, J., Vázquez-Semadeni, E., et al. 2015, MNRAS, 453, 3785
Palau, A., Zapata, L. A., Román-Zúñiga, C. G., et al. 2018, ApJ, 855, 24
Peretto, N., Fuller, G. A., Duarte-Cabral, A., et al. 2013, A&A, 555, A112
Pety, J. 2005, in SF2A-2005: Semaine de l'Astrophysique Francaise, ed. F. Casoli et al. (Les Ulis: EDP), 721
Pineda, J. E., Rosolowsky, E. W., & Goodman, A. A. 2009, ApJL, 699, L134
Rathborne, J. M., Whitaker, J. S., Jackson, J. M., et al. 2016, PASA, 33, E030
Remijan, A., Sutton, E. C., Snyder, L. E., et al. 2004, ApJ, 606, 917
Rieke, G. H., Young, E. T., Engelbracht, C. W., et al. 2004, ApJS, 154, 25
Robitaille, T. P., Meade, M. R., Babler, B. L., et al. 2008, AJ, 136, 2413
Rosolowsky, E. W., Pineda, J. E., Kauffmann, J., & Goodman, A. A. 2008, ApJ, 679, 1338
Sánchez-Monge, Á, Beltrán, M. T., Cesaroni, R., et al. 2013, A&A, 550, A21
Sanhueza, P., Contreras, Y., Wu, B., et al. 2019, ApJ, 886, 102
Sanhueza, P., Jackson, J. M., Foster, J. B., et al. 2012, ApJ, 756, 60
Sanhueza, P., Jackson, J. M., Zhang, Q., et al. 2017, ApJ, 841, 97
Sault, R. J., Teuben, P. J., & Wright, M. C. H. 1995, in ASP Conf. Ser. 77, Astronomical Data Analysis Software and Systems IV, ed. R. A. Shaw, H. E. Payne, & J. J. E. Hayes (San Francisco, CA: ASP), 433
Schneider, S., & Elmegreen, B. G. 1979, ApJS, 41, 87
Schuller, F., Menten, K. M., Contreras, Y., et al. 2009, A&A, 504, 415
Servajean, E., Garay, G., Rathborne, J., Contreras, Y., & Gómez, L. 2019, ApJ, 878, 146
Sutton, E. C., Peng, R., Danchi, W. C., et al. 1995, ApJS, 97, 455
Takahashi, S., Ho, P. T. P., Teixeira, P. S., Zapata, L. A., & Su, Y.-N. 2013, ApJ, 763, 57
Tan, J. C., Beltrán, M. T., Caselli, P., et al. 2014, in Protostars and Planets VI, Vol. 149, ed. H. Beuther et al. (Tucson, AZ: Univ. Arizona Press)
Teixeira, P. S., Takahashi, S., Zapata, L. A., & Ho, P. T. P. 2016, A&A, 587, A47
Turner, B. E. 1991, ApJS, 76, 617
Urquhart, J. S., Csengeri, T., Wyrowski, F., et al. 2014, A&A, 568, A41
Vázquez-Semadeni, E., Gómez, G. C., Jappsen, A. K., Ballesteros-Paredes, J., & Klessen, R. S. 2009, ApJ, 707, 1023
Vázquez-Semadeni, E., González-Samaniego, A., & Colín, P. 2017, MNRAS, 467, 1313
Virtanen, P., Gommers, R., Oliphant, T. E., et al. 2019, arXiv:1907.10121
Whitaker, J. S., Jackson, J. M., Rathborne, J. M., et al. 2017, AJ, 154, 140
Whitworth, A. P., & Ward-Thompson, D. 2001, ApJ, 547, 317
Williams, J. P., de Geus, E. J., & Blitz, L. 1994, ApJ, 428, 693
Zhang, Q., Wang, K., Lu, X., & Jiménez-Serra, I. 2015, ApJ, 804, 141